

***Euclid*: Constraining linearly scale-independent modifications of gravity with the spectroscopic and photometric primary probes[★]**

N. Frusciante^{1**}, F. Pace^{2,3,4}, V.F. Cardone^{5,6}, S. Casas⁷, I. Tutusaus^{8,9,10,11}, M. Ballardini^{12,13,14,15}, E. Bellini^{16,17,18,8}, G. Benevento¹⁹, B. Bose^{20,8,21}, P. Valageas²², N. Bartolo^{23,24,25}, P. Brax^{22,26}, P. G. Ferreira²⁷, F. Finelli^{14,28}, K. Koyama²⁹, L. Legrand⁸, L. Lombriser⁸, D. Paoletti^{14,15}, M. Pietroni^{30,31}, A. Rozas-Fernández³², Z. Sakr^{33,34,35}, A. Silvestri³⁶, F. Vernizzi²², H.A. Winther³⁷, N. Aghanim³⁸, L. Amendola³⁴, N. Auricchio¹⁴, R. Azzollini³⁹, M. Baldi^{13,14,15}, D. Bonino⁴, E. Branchini^{40,41}, M. Brescia^{1,42}, J. Brinchmann⁴³, S. Camera^{2,3,4}, V. Capobianco⁴, C. Carbone⁴⁴, J. Carretero^{45,46}, M. Castellano⁵, S. Cavuoti^{42,47}, A. Cimatti^{48,49}, R. Cledassou^{50,51}, G. Congedo²⁰, L. Conversi^{52,53}, Y. Copin⁵⁴, L. Corcione⁴, F. Courbin⁵⁵, M. Cropper³⁹, A. Da Silva^{56,32}, H. Degaudenzi⁵⁷, J. Dinis^{32,56}, F. Dubath⁵⁷, X. Dupac⁵³, S. Dusini²⁴, S. Farrens⁵⁸, S. Ferriol⁵⁴, P. Fosalba^{10,9}, M. Frailis⁵⁹, E. Franceschi¹⁴, S. Galeotta⁵⁹, B. Gillis²⁰, C. Giocoli^{14,60}, A. Grazian²⁵, F. Grupp^{61,62}, L. Guzzo^{63,64,65}, S.V.H. Haugan³⁷, W. Holmes⁶⁶, F. Hormuth⁶⁷, A. Hornstrup⁶⁸, K. Jahnke⁶⁹, S. Kermiche⁷⁰, A. Kiessling⁶⁶, M. Kilbinger⁵⁸, T. Kitching³⁹, M. Kunz⁸, H. Kurki-Suonio⁷¹, S. Ligorì⁴, P. B. Lilje³⁷, I. Lloro⁷², E. Maiorano¹⁴, O. Mansutti⁵⁹, O. Marggraf⁷³, K. Markovic⁶⁶, F. Marulli^{74,14,15}, R. Massey⁷⁵, E. Medinaceli¹⁴, M. Meneghetti^{15,14}, G. Meylan⁵⁵, M. Moresco^{74,14}, L. Moscardini^{74,14,15}, E. Munari⁵⁹, S.M. Niemi⁷⁶, J. Nightingale⁷⁵, C. Padilla⁴⁵, S. Paltani⁵⁷, F. Pasian⁵⁹, K. Pedersen⁷⁷, W.J. Percival^{78,79,80}, V. Pettorino⁵⁸, G. Polenta⁸¹, M. Poncet⁵⁰, L. Popa⁸², F. Raison⁶¹, R. Rebolo^{83,84}, A. Renzi^{23,24}, J. Rhodes⁶⁶, G. Riccio⁴², E. Romelli⁵⁹, R. Saglia^{61,62}, D. Sapone⁸⁵, B. Sartoris^{62,59}, A. Secroun⁷⁰, G. Seidel⁶⁹, C. Sirignano^{23,24}, G. Sirri¹⁵, L. Stanco²⁴, C. Surace⁸⁶, P. Tallada-Crespi^{87,46}, A.N. Taylor²⁰, I. Tereno^{56,88}, R. Toledo-Moreo⁸⁹, F. Torradeflot^{87,46}, E.A. Valentijn⁹⁰, L. Valenziano^{14,28}, T. Vassallo⁵⁹, G.A. Verdoes Kleijn⁹⁰, Y. Wang⁹¹, A. Zacchei⁵⁹, G. Zamorani¹⁴, J. Zoubian⁷⁰, V. Scottez⁹²

(Affiliations can be found after the references)

June 22, 2023

ABSTRACT

Context. The future *Euclid* space satellite mission will offer an invaluable opportunity to constrain modifications to Einstein's general relativity at cosmic scales. In this paper we focus on modified gravity models characterised, at linear scales, by a scale-independent growth of perturbations while featuring different testable types of derivative screening mechanisms at smaller nonlinear scales.

Aims. We consider three specific models, namely Jordan-Brans-Dicke (JBD), a scalar-tensor theory with a flat potential, the normal branch of Dvali-Gabadadze-Porrati (nDGP) gravity, a braneworld model in which our Universe is a four-dimensional brane embedded in a five-dimensional Minkowski space-time, and *k*-mouflage (KM) gravity, an extension of *k*-essence scenarios with a universal coupling of the scalar field to matter. In preparation for real data, we provide forecasts from spectroscopic and photometric primary probes by *Euclid* on the cosmological parameters and the extra parameters of the models, respectively, ω_{BD} , Ω_{rc} and $\epsilon_{2,0}$, which quantify the deviations from general relativity. This analysis will improve our knowledge of the cosmology of these modified gravity models.

Methods. The forecasts analysis employs the Fisher matrix method applied to weak lensing (WL); photometric galaxy clustering (GC_{ph}); spectroscopic galaxy clustering (GC_{sp}) and the cross-correlation (XC) between GC_{ph} and WL. For the *Euclid* survey specifications we define three scenarios, characterised by different cuts in the maximum multipole and wavenumber, to assess the constraining power of nonlinear scales. For each model we consider two fiducial values for the corresponding model parameter.

Results. In an optimistic setting at 68.3% confidence interval, with *Euclid* alone we find the following percentage relative errors: for $\log_{10} \omega_{\text{BD}}$, with a fiducial value of $\omega_{\text{BD}} = 800$, 35% using GC_{sp} alone, 3.6% using GC_{ph}+WL+XC and 3.3% using GC_{ph}+WL+XC+GC_{sp}; for $\log_{10} \Omega_{\text{rc}}$, with a fiducial value of $\Omega_{\text{rc}} = 0.25$, we find respectively 90%, 20% and 17%; finally, for $\epsilon_{2,0} = -0.04$ respectively 5%, 0.15% and 0.14%. From the relative errors for fiducial values closer to their Λ CDM limits, we find that most of the constraining power is lost. Our results highlight the importance of the constraining power coming from nonlinear scales.

Key words. Gravitational lensing: weak – large-scale structure of Universe – cosmological parameters

1. Introduction

We have entered a new era in gravitational physics where it is now possible to test and exploit general relativity (GR) on a wide range of scales. The successes of Solar System constraints, and

the precision measurements arising from observations of millisecond pulsars can now be combined with detections of gravitational waves and images of black hole shadows (Berti et al. 2015). To this battery of techniques one must add cosmological constraints using the large scale structure of the Universe (Ferreira 2019).

[★] This paper is published on behalf of the Euclid Consortium.

^{**} e-mail: noemi.frusciante@unina.it

There have been multiple attempts at constraining GR with cosmological surveys (Aghanim et al. 2020; Mueller et al. 2018; Joudaki et al. 2018; Lee et al. 2021; Raveri et al. 2021). Using spectroscopic and imaging surveys of galaxies, combined with measurements of the cosmic microwave background (CMB) it has been possible to map out gravitational potentials over an appreciable part of the universe as well as pin down the growth rate of structure and its morphology out to redshift $z \sim 2$. The resulting constraints have been an important first step in understanding gravity in an altogether untested regime yet they have been underwhelming. For example, constraints on the simplest scalar-tensor modification to GR – Jordan-Brans-Dicke (JBD) gravity – are more than order of magnitude weaker (Joudaki et al. 2022; Ballardini et al. 2022) than those obtained from millisecond pulsar observations (Voisin et al. 2020), albeit on very different scales.

The relevance of cosmological measurements for gravitational physics is about to change with the upcoming generation of large-scale structure surveys (Ferreira 2019). By mapping out vast swathes of the Universe with exquisite precision, one hopes that it will be possible to tighten substantially constraints on gravitational physics on the largest observable scales. Of particular importance in this new vanguard is the *Euclid* mission. The *Euclid* satellite will undertake two key, complementary surveys – a spectroscopic survey of galaxies and an imaging survey (targeting weak lensing and which can also be used to reconstruct galaxy clustering using photometric redshifts) – with a primary goal of pinning down the nature of dark energy and ideally suited for cosmological constraints on gravity (Euclid Collaboration: Blanchard et al. 2020, EC19 hereafter).

Given the potential of the *Euclid* mission it is imperative to assess its ability to constrain GR. One way of doing so is by assessing how well it will be able to constrain specific extensions of GR, in particular modified gravity models (MG). MG models are particularly constrained by small scale experiments such as the ones in the Solar System where fifth-force effects (Bertotti et al. 2003) and a violation of the equivalence principle (Williams et al. 2012; Touboul et al. 2017) have been thoroughly investigated. As a result, extensions of GR which preserve the equivalence principle in the Earth’s environment and exclude large fifth-force effects on Solar System scales must shield small scales from potential deviations from GR on large cosmological distances. New physical effects would only reveal themselves on large scales where the *Euclid* mission would have the potential to unravel them. Screening of GR extensions have been broadly classified into three families: the chameleon (Khouri & Weltman 2004), k -mouflage (Babichev et al. 2009) and Vainshtein (Vainshtein 1972) mechanisms (see, for a recent review, Brax et al. 2021). For chameleons, screening occurs in regions of space where Newton’s potential is large enough whilst for k -mouflage and Vainshtein this takes place where the first or second spatial derivatives of Newton’s potential are also large enough. One particular example of an extensively studied theory with the chameleon screening property is $f(R)$ gravity (Carroll et al. 2004; Hu & Sawicki 2007b). It has been shown that the *Euclid* mission, using the combination of spectroscopic and photometric probes, will be able to distinguish this model from Λ CDM at more than 3σ confidence level, for realistic fiducial values of its free model parameter, f_{R0} (Casas et al. 2023). Derivative screening mechanisms, i.e. k -mouflage and Vainshtein, have not been investigated within the context of the *Euclid* mission and this will be one of the outcomes of the present work.

In this paper we will forecast how well the surveys from the *Euclid* mission can be used to constrain a family of theories that

modify the theory of GR yet retain one of its properties: a scale-independent linear growth rate. The three theories we will consider are: JBD gravity (Brans & Dicke 1961), the simplest scalar-tensor theory which involves a non-minimal coupling between a scalar field and the metric; Dvali-Gabadadze-Porrati gravity (DGP, see Dvali et al. 2000), a braneworld model which introduces modifications on cosmological scales and screens with the Vainshtein mechanism; a k -mouflage model (KM, see Babichev et al. 2009; Brax & Valageas 2014, 2016), i.e. a scalar-tensor theory with a non-canonical kinetic energy and the k -mouflage screening property. The JBD theory is not screened and, therefore, suffers from large deviations from GR unless the Brans-Dicke (BD) parameter $\omega_{BD} > 4 \times 10^4$ (Bertotti et al. 2003). This is larger than the range of parameters testable cosmologically as we shall see below implying that the JBD model investigated here must be taken as a template for large scale deviations against which we compare the DGP and k -mouflage models. All these modifications of GR will, in one way or another, affect the expansion rate and growth of structure and are, thus, prime candidates to be constrained by data from the *Euclid* mission.

We structure this paper as follows. In Sect. 2 we recap the essential facts about linear cosmological perturbations in the context of extensions to GR, identifying the phenomenological time-dependent parameters, $(\mu, \eta$ and $\Sigma)$, that are fed into the linear evolution equations. We then delve into the three candidate theories we are exploring, laying out their corresponding actions, background evolution, functional forms of $\{\mu, \eta$ and $\Sigma\}$ and how all this is implemented numerically. In Sect. 3 we present a detailed explanation of how we calculate all aspects of the theoretical model predictions that will go into the forecasting procedure. In Sect. 4 we describe the survey specifications and how these are integrated in the analysis method; in this paper we will be using a Fisher forecasting approach. In Sect. 5 we present the results of our methods and in Sect. 6 we conclude.

2. Linearly scale-independent modified gravity

We follow the Bardeen formalism (Bardeen 1980; Ma & Bertschinger 1995), and define the infinitesimal line element of the flat Friedmann-Lemaître-Robertson-Walker (FLRW) metric by

$$ds^2 = -(1 + 2\Psi)c^2 dt^2 + a^2(t)(1 - 2\Phi)\delta_{ij} dx^i dx^j, \quad (1)$$

where $a(t)$ is the scale factor as a function of the cosmic time t , Ψ and Φ are the two scalar potentials and c the speed of light. We will work in Fourier space, where modes are functions of t and the comoving wavenumber k^i . At linear order, the matter energy-momentum tensor can be decomposed as follows,

$$T_0^0 = -\bar{\rho}(1 + \delta)c^2, \quad T_i^0 = (\bar{\rho} + \bar{p}/c^2)cv_i, \quad T_j^i = (\bar{p} + \delta p)\delta_j^i + \Sigma_j^i, \quad (2)$$

where $\delta = \rho/\bar{\rho} - 1$ is the energy density contrast with ρ being the matter density and $\bar{\rho}$ its background value, $p = \bar{p} + \delta p$ is the pressure with \bar{p} the background value, v_i is the peculiar velocity and Σ_j^i is the (traceless) anisotropic stress, $\Sigma_i^i = 0$. In the following we work with the scalar component of the matter anisotropic stress and the comoving density perturbation, respectively defined as $(\bar{\rho}c^2 + \bar{p})(\hat{k}^i \cdot \hat{k}_j - 1/3\delta_j^i)\sigma = \Sigma_j^i$ with $\hat{k}_i = k_i/k$ and $\bar{\rho}\Delta \equiv \bar{\rho}\delta + 3(aH/k/c^2)(\bar{\rho} + \bar{p}/c^2)v$, where v is the velocity potential defined through $v_i = -ik_i v/k$. Here $H \equiv \dot{a}/a$ is the Hubble function and a dot stands for the derivative with respect to the cosmic time. In analogy to the Λ CDM model where curvature is found to be compatible with zero, in this work we will assume a flat spatial geometry.

In models where gravity is modified by the presence of a scalar field, the relations between the gravitational potentials and the matter perturbations are modified. These deviations from GR can be encoded into two functions, defined as follows:

$$-k^2\Psi = \frac{4\pi G_N}{c^2} a^2\mu(a, k) [\bar{\rho}\Delta + 3(\bar{\rho} + \bar{p}/c^2)\sigma], \quad (3)$$

$$-k^2(\Phi + \Psi) = \frac{8\pi G_N}{c^2} a^2\{\Sigma(a, k) [\bar{\rho}\Delta + 3(\bar{\rho} + \bar{p}/c^2)\sigma] - \frac{3}{2}\mu(a, k)(\bar{\rho} + \bar{p}/c^2)\sigma\}, \quad (4)$$

where G_N is Newton's gravitational constant and c the speed of light. As such, a further function that can be introduced is the one defining the ratio of the two potentials, $\eta = \Phi/\Psi$. In the absence of anisotropic stress the three phenomenological functions are related by the following expression:

$$\Sigma = \frac{1}{2}\mu(1 + \eta). \quad (5)$$

The *phenomenological functions* μ , η and Σ are identically equal to 1 in the GR limit. In general they are functions of time and scale. The models that we consider in this paper preserve the scale-independent (linear) growth pattern, i.e. they have $\mu = \mu(a)$, $\Sigma = \Sigma(a)$ and $\eta = \eta(a)$.

For a given theory, μ and Σ can be determined numerically, after solving for the full dynamics of linear perturbations via an Einstein-Boltzmann solver. This can be achieved with `hi_class` (Zumalacárregui et al. 2017; Bellini et al. 2020) or `EFTCAMB` (Hu et al. 2014; Raveri et al. 2014), which implements the effective field theory formalism for dark energy into the standard `CLASS` (Blas et al. 2011; Lesgourgues 2011) and `CAMB` (Lewis et al. 2000) codes, respectively. These codes have been validated as part of an extended code comparison effort (Bellini et al. 2018). Alternatively, one can opt for the quasi-static (QS) limit, i.e., scales sufficiently small to be well within the horizon and the sound-horizon of the scalar field, and derive the phenomenological functions analytically. In this case, one can use the `MGCAMB` patch to `CAMB` (Zhao et al. 2009; Hojjati et al. 2011; Zucca et al. 2019).

In the following, we will introduce the three models under consideration, i.e., JBD, DGP and KM. We will provide the background evolution equations and the expressions for μ , η and Σ for each of these models.

2.1. Jordan-Brans-Dicke gravity

The Jordan-Brans-Dicke theory of gravity (Brans & Dicke 1961) is described by the following action,

$$S_{\text{BD}} = \int d^4x \sqrt{-g} \left[\frac{c^4}{16\pi} \left(\phi R - \frac{\omega_{\text{BD}}}{\phi} g^{\mu\nu} \partial_\mu \phi \partial_\nu \phi - 2\Lambda \right) + \mathcal{L}_m \right], \quad (6)$$

where $g_{\mu\nu}$ is the metric and R its associated Ricci scalar, ϕ is the JBD scalar field (which has the dimensions of the inverse of Newton's constant), ω_{BD} is the dimensionless BD parameter, and \mathcal{L}_m is the matter Lagrangian which is minimally coupled to the metric. We have included a cosmological constant, Λ . The model has only one free parameter, ω_{BD} ; in the limit in which $\omega_{\text{BD}} \rightarrow \infty$, the scalar field is frozen and we recover Einstein gravity.

The JBD theory of gravity is remarkably simple in that it depends on so few parameters. Yet, cosmological constraints

on JBD gravity can have wider implications if one takes the view that it is the long-wavelength, low-energy limit of more general scalar-tensor theories (see Joudaki et al. 2022, for example). Furthermore, more general scalar theories may be endowed with gravitational screening which will kick in on smaller scales or, alternatively, regions of high density, for example. As a consequence local constraints will, to some extent, decouple from more global, or large scale, constraints. Thus, constraints on cosmological scales on JBD theory may cover a broad class of scalar-tensor theories and, furthermore, be independent from model specific constraints on small scales. Thus, while simple, JBD gravity is a powerful tool for constraining general classes of scalar-tensor theories using cosmological data.

The modified Einstein field equations are

$$G_{\mu\nu} = \frac{8\pi}{c^4} \frac{1}{\phi} T_{\mu\nu} + \frac{\omega_{\text{BD}}}{\phi^2} \left(\nabla_\mu \phi \nabla_\nu \phi - \frac{1}{2} g_{\mu\nu} \nabla_\alpha \phi \nabla^\alpha \phi \right) + \frac{1}{\phi} \left[\nabla_\mu \nabla_\nu \phi - g_{\mu\nu} (\square \phi + \Lambda) \right]. \quad (7)$$

Here $T_{\mu\nu}$ is the total matter stress-energy tensor while \square denotes the d'Alembertian. On the background, these equations give

$$3H^2 = \frac{8\pi \bar{\rho}}{c^4 \phi} - 3H \frac{\dot{\phi}}{\phi} + \frac{\omega_{\text{BD}}}{2} \frac{\dot{\phi}^2}{\phi^2} + \frac{\Lambda}{\phi}, \quad (8)$$

$$2\dot{H} + 3H^2 = -\frac{8\pi \bar{p}}{c^4 \phi} - \frac{\omega_{\text{BD}}}{2} \frac{\dot{\phi}^2}{\phi^2} - 2H \frac{\dot{\phi}}{\phi} - \frac{\ddot{\phi}}{\phi} + \frac{\Lambda}{\phi}, \quad (9)$$

and the scalar field equation of motion reads

$$\square \phi = \frac{8\pi}{c^4} \left(\frac{T}{3 + 2\omega_{\text{BD}}} \right) - \frac{4\Lambda}{3 + 2\omega_{\text{BD}}}, \quad (10)$$

where $T \equiv g^{\mu\nu} T_{\mu\nu}$ is the trace of the stress-energy tensor on the background.

The phenomenological QS functions in this theory read

$$\begin{aligned} \Sigma &= \frac{1}{G_N \phi}, \\ \mu &= \frac{4 + 2\omega_{\text{BD}}}{3 + 2\omega_{\text{BD}}} \Sigma, \\ \eta &\equiv \frac{\Phi}{\Psi} = \frac{1 + \omega_{\text{BD}}}{2 + \omega_{\text{BD}}}. \end{aligned} \quad (11)$$

Constraints on JBD gravity have been obtained by using a combination of different cosmological data sets and sampling over different parameterisation of the BD parameter ω_{BD} . For example, Avilez & Skordis (2014) imposed a flat prior on $-\log_{10}(\omega_{\text{BD}})$ to obtain a lower bound of $\omega_{\text{BD}} > 1900$ at 95% CL with CMB information from *Planck* 2013 data. Ballardini et al. (2016) obtained $\log_{10}(1 + 1/\omega_{\text{BD}}) < 0.0030$ at 95% CL combining *Planck* 2015 and BOSS DR10-11 data; this upper bound was subsequently updated in Ballardini et al. (2020) with a combination of *Planck* 2018 and BOSS DR12 data to $\log_{10}(1 + 1/\omega_{\text{BD}}) < 0.0022$ at 95% CL. Joudaki et al. (2022) used a combination of the *Planck* 2018 CMB data, the $3 \times 2\text{pt}$ combination of the KiDS and 2dFLens data, the Pantheon supernovae data, BOSS measurements of the BAO, to find the coupling constant $\omega_{\text{BD}} > \{1540, 160, 160, 350\}$ at 95% CL for the different choices of parametrization (or priors): $\{\log_{10}(1/\omega_{\text{BD}}), \log_{10}(1 + 1/\omega_{\text{BD}}), 1/\omega_{\text{BD}}, 1/\log_{10} \omega_{\text{BD}}\}$. These constraints were obtained fixing the value of the scalar field today to

$$G_N \phi(a=1) = \frac{2\omega_{\text{BD}} + 4}{2\omega_{\text{BD}} + 3}, \quad (12)$$

in order to guarantee that the effective gravitational constant at present corresponds with the one measured in a Cavendish-like experiment (Boisseau et al. 2000). See also Avilez & Skordis (2014); Joudaki et al. (2022); Ballardini et al. (2022) for studies of the JBD model without imposing this condition and Ballardini et al. (2016); Ooba et al. (2017); Rossi et al. (2019); Braglia et al. (2020, 2021); Cheng et al. (2021) for a simple generalization of these constraints extending the JBD action (6) with different potentials and couplings to the Ricci scalar.

The JBD model is implemented in CLASSig (Umiltà et al. 2015) and hi_class (Zumalacárregui et al. 2017; Bellini et al. 2020). For these codes the agreement and validation of the background and linear perturbations was thoroughly studied in Bellini et al. (2018). In this paper we use the results produced with hi_class.

2.2. Dvali-Gabadadze-Porrati braneworld gravity

The Dvali-Gabadadze-Porrati model (Dvali et al. 2000) is a five-dimensional braneworld model defined by the action

$$S = \frac{c^4}{16\pi G_5} \int_{\mathcal{M}} d^5x \sqrt{-\gamma} R_5 + \int_{\partial\mathcal{M}} d^4x \sqrt{-g} \left[\frac{c^4}{16\pi G_N} R + \mathcal{L}_m \right], \quad (13)$$

where γ is the five-dimensional metric and R_5 its Ricci curvature scalar. G_5 and G_N are the five- and four-dimensional Newton's constants, respectively. The matter Lagrangian is denoted with \mathcal{L}_m and is confined to a four-dimensional brane in a five-dimensional Minkowski spacetime. The induced gravity described by the usual four-dimensional Einstein-Hilbert action is responsible for the recovery of the four-dimensional gravity on the brane. The cross-over scale $r_c = G_5/(2G_N)$ is the only parameter of the model and GR is recovered in the limit $r_c \rightarrow \infty$.

The Friedmann equation on the brane is given by (Deffayet 2001)

$$H^2 = \pm c \frac{H}{r_c} + \frac{8\pi G}{3} \bar{\rho}. \quad (14)$$

There are two branches of solutions depending on the embedding of the brane: the self-accelerating branch (sDGP, Bowcock et al. 2000; Deffayet 2001) and the normal branch (nDGP, Bowcock et al. 2000; Deffayet 2001), corresponding to the + and - sign for the contribution from the five-dimensional gravity, respectively. The self-accelerating branch admits the late-time acceleration without dark energy but the solution is plagued by ghost instabilities (Luty et al. 2003; Gorbunov et al. 2006; Charmousis et al. 2006). Thus we focus on the normal branch. In order to separate the effect of MG on structure formation from that on the expansion history, it is often assumed that the background expansion is identical to that of Λ CDM. This can be achieved by introducing an additional dark energy contribution with an appropriate equation of state (Schmidt 2009; Bag et al. 2018). We will adopt this approach.

The evolution of density and metric perturbations on the brane require solutions of the bulk metric equations. These bulk effects can be encapsulated in an effective $3+1$ description that uses the combination of any two of the functions μ , η , Σ . Using the results of Koyama & Maartens (2006); Hu & Sawicki (2007a); Song (2008); Cardoso et al. (2008); Lombriser et al. (2009); Seahra & Hu (2010), we have

$$\eta = \frac{1+g}{1-g}, \quad (15)$$

where, using the quasi-static (QS) approximation, we have (Lombriser et al. 2013)

$$g(a) = g_{\text{QS}} = -\frac{1}{3} \left[1 \mp \frac{2Hr_c}{c} \left(1 + \frac{\dot{H}}{3H^2} \right) \right]^{-1}, \quad (16)$$

such that the effective modification introduced with η can be treated as scale-independent.

The effective $3+1$ Poisson equation for the lensing potential in the QS approximation is

$$-k^2(\Phi + \Psi) = \frac{8\pi G_N}{c^2} a^2 \bar{\rho} \Delta, \quad (17)$$

therefore (Lombriser et al. 2013)

$$\Sigma = 1, \quad (18)$$

and hence

$$\mu(a) = 1 + \frac{1}{3\beta}, \quad \beta(a) \equiv 1 + \frac{H}{H_0} \frac{1}{\sqrt{\Omega_{\text{rc}}}} \left(1 + \frac{\dot{H}}{3H^2} \right). \quad (19)$$

We have chosen to parameterise the modification to gravity by $\Omega_{\text{rc}} \equiv c^2/(4r_c^2 H_0^2)$.

There are not many studies on constraining nDGP with an exact Λ CDM background. However, Raccanelli et al. (2013), using measurements of the zeroth and second order moments of the correlation function from SDSS DR7 data up to $r_{\text{max}} = 120 \text{ Mpc } h^{-1}$, and marginalized bias, found an Ω_{rc} upper limit at 95% of ~ 40 (from $r_c > 340 \text{ Mpc}$ with fixed $H_0 = 70 \text{ km s}^{-1} \text{ Mpc}^{-1}$). In addition, Barreira et al. (2016) used clustering wedges statistic of the galaxy correlation function and the growth rate values estimated from more recent BOSS DR12 data to set $[r_c H_0/c]^{-1} < 0.97$ at 95% C.L., corresponding to an upper bound of $\Omega_{\text{rc}} < 0.27$.

There have also been recent attempts to forecast Ω_{rc} . Liu et al. (2021), using galaxy cluster abundance from the Simons Observatory and galaxy correlation functions from a DESI-like experiment, found $\delta(\Omega_{\text{rc}}) \sim 0.038$ around a fiducial value of 0.25. Cataneo et al. (2022) forecast for *Euclid*-like future constraints on a fiducial $\Omega_{\text{rc}} \sim 0.0625$ a 1σ accuracy of 0.0125 from combining the 3D matter power spectrum and the probability distribution function of the smoothed three-dimensional matter density field probes. Also Bose et al. (2020) forecast for a LSST-like survey, using cosmic shear alone, on a fiducial $\Omega_{\text{rc}} \sim 0$ a 1σ accuracy of 0.08.

Note that constraints have also been inferred for a nDGP model with cosmological constant rather than a constructed dark energy field, thus with an approximate Λ CDM background. For this model, Lombriser et al. (2009) and Xu (2014) inferred somewhat stronger constraints of $\Omega_{\text{rc}} < 0.020$ (95% C.L.) and $\Omega_{\text{rc}} < 0.002$ (68% C.L.) from the combination of CMB and large-scale structure data, where the constraints are mainly driven by the CMB data. Thus, high-precision CMB measurements such as by the Planck satellite tightly constrain Ω_{rc} . In this work we focus on the model with the exact Λ CDM background as our interest is to see how *Euclid* can constrain the modification in structure formation that is not coming from a different background.

nDGP has been implemented in MGCAMB and in QSA_CLASS (Pace et al. 2021). These codes solve for a Λ CDM-background evolution and Eqs. (18) and (19). The overall agreement in the linear matter power spectrum is never worse than 0.5%. In this paper we use the results produced with MGCAMB.

2.3. *k-mouflage* gravity

k-mouflage theories are built complementing simple *k*-essence scenarios with a universal coupling of the scalar field φ to matter. They are defined by the action (Babichev et al. 2009; Brax & Valageas 2014, 2016)

$$S = \int d^4x \sqrt{-\tilde{g}} \left[\frac{c^4}{16\pi\tilde{G}_N} \tilde{R} + c^2 \mathcal{M}^4 K(\tilde{\chi}) \right] + S_m(\psi_i, g_{\mu\nu}), \quad (20)$$

where \tilde{G}_N is the bare Newton constant, \mathcal{M}^4 is the energy density scale of the scalar field, $g_{\mu\nu}$ is the Jordan frame metric, $\tilde{g}_{\mu\nu}$ is the Einstein frame metric with $g_{\mu\nu} = A^2(\varphi)\tilde{g}_{\mu\nu}$, S_m is the Lagrangian of the matter fields $\psi_m^{(i)}$, $\tilde{\chi}$ is defined as

$$\tilde{\chi} = -\frac{\tilde{g}^{\mu\nu}\partial_\mu\varphi\partial_\nu\varphi}{2\mathcal{M}^4}, \quad (21)$$

and $\mathcal{M}^4 K$ is the non-standard kinetic term of the scalar field.

In these theories the evolution of both the background and perturbations is affected by the universal coupling and by the scalar field dynamics. The amount of deviation from Λ CDM at the background level and in perturbation theory can be expressed in terms of two time-dependent functions, related to the coupling A and the kinetic function K , i.e.,

$$\epsilon_2 \equiv \frac{d \ln \bar{A}}{d \ln a}, \quad \epsilon_1 \equiv \frac{2}{\bar{K}'} \left[\epsilon_2 \frac{c}{\sqrt{8\pi\tilde{G}_N}} \left(\frac{d\tilde{\varphi}}{d \ln a} \right)^{-1} \right]^2, \quad (22)$$

where over-bars denote background quantities and a prime indicates derivatives w.r.t. $\tilde{\chi}$. The KM Friedmann equation therefore reads

$$H^2 = \frac{8\pi\tilde{G}_N}{3} \frac{\bar{A}^2}{(1-\epsilon_2)^2} \left[\bar{\rho} + \frac{\mathcal{M}^4}{\bar{A}^4} \left(2\tilde{\chi} \frac{d\bar{K}}{d\tilde{\chi}} - \bar{K} \right) \right]. \quad (23)$$

Considering linear scalar perturbations around an FLRW background, the phenomenological functions μ and Σ read (Benevento et al. 2019):

$$\mu(a) = (1 + \epsilon_1)\bar{A}^2, \quad \Sigma(a) = \bar{A}^2. \quad (24)$$

We recover GR when $\epsilon_1 \rightarrow 0$, $\epsilon_2 \rightarrow 0$, and A and K are constants, with $\mathcal{M}^4 K$ playing the role of the cosmological constant, see Eq. (20).

In addition to the six standard Λ CDM parameters, the KM model requires the specification of the kinetic function $K(\tilde{\chi})$ and of the coupling $A(\varphi)$. Following Brax & Valageas (2016), this can also be expressed in terms of the time-dependent background values $\bar{K}(a)$ and $\bar{A}(a)$. Brax & Valageas (2016) proposed a simple parameterization that satisfies self-consistency constraints. It involves five parameters, $\{\epsilon_{2,0}, \gamma_A, m, \alpha_U, \gamma_U\}$, where $\epsilon_{2,0}$ is the value of ϵ_2 at redshift $z = 0$ and must be negative to ensure there are no ghosts in the theory. For the coupling function $\bar{A}(a)$, this reads

$$\bar{A}(a) = 1 + \alpha_A - \alpha_A \left[\frac{(\gamma_A + 1)a}{\gamma_A + a} \right]^{\gamma_A}, \quad (25)$$

with

$$\nu_A = \frac{3(m-1)}{2m-1}, \quad \alpha_A = -\frac{\epsilon_{2,0}(1+\gamma_A)}{\gamma_A \nu_A}. \quad (26)$$

Here, m is the exponent of the kinetic function for large argument, $K \sim \tilde{\chi}^m$, which also specifies the high-redshift dependence of $\bar{A}(a)$, while γ_A sets the redshift where \bar{A} goes from the current

unit value to the high-redshift value $1 + \alpha_A$, which is parameterized by $\epsilon_{2,0}$. The background kinetic function $\bar{K}(a)$ is conveniently parameterized in terms of a function $U(a)$, with

$$\frac{d\bar{K}'}{d\tilde{\chi}} = \frac{U(a)}{a^3 \sqrt{\tilde{\chi}}}, \quad \sqrt{\tilde{\chi}} = -\frac{\bar{\rho}_0}{\mathcal{M}^4} \frac{\epsilon_2 \bar{A}^4}{2U(-3\epsilon_2 + \frac{d \ln U}{d \ln a})}, \quad (27)$$

which we take to be of the form

$$U(a) \propto \frac{a^2 \ln(\gamma_U + a)}{(\sqrt{a_{\text{eq}}} + \sqrt{a}) \ln(\gamma_U + a) + \alpha_U a^2}. \quad (28)$$

The various terms in this expression allow us to follow the radiation, matter and dark-energy eras. The parameters α_U and γ_U , of order unity, set the shape of the transition to the dark-energy era. The main parameter is $\epsilon_{2,0}$, which measures the amplitude of the deviation from GR and Λ CDM at $z = 0$. Other parameters, of order unity, mostly describe the shapes of the transitions between different cosmological regimes.

The KM model has been tested against a set of complementary cosmological data sets, including CMB temperature, polarization and lensing, type Ia Supernovae, baryon acoustic oscillations (BAO) and local measurements of H_0 (Benevento et al. 2019). This gives the 95% C.L. bounds $-0.04 \leq \epsilon_{2,0} \leq 0$, while the other parameters are unconstrained (as long as they do not become very large). These results are consistent with earlier more qualitative CMB studies (Barreira et al. 2015). The X-ray cluster multiplicity function could provide bounds of the same order (Brax et al. 2015), but more detailed analysis are needed to derive robust constraints.

The fact that $\epsilon_{2,0}$ is the main parameter constrained by the data can be understood from Eqs. (22) and (24) and the property that at leading order over ϵ_2 , we have $\epsilon_1 \simeq -\epsilon_2$. Indeed, this shows that the running of Newton's constant and the impact on the linear metric and matter density fluctuations are set by ϵ_2 . Because most of the deviations from Λ CDM occur at low redshift, this is mostly determined by the value $\epsilon_{2,0}$ at $z = 0$. Therefore, in this work we focus on the dependence on $\epsilon_{2,0}$, which is left free to vary, while we fix the other parameters to $\gamma_A = 0.2$, $m = 3$, $\alpha_U = 0.2$, and $\gamma_U = 1$, as some representative values for the other parameters. Thus, this gives one additional parameter, $\epsilon_{2,0}$, in addition to the six standard Λ CDM parameters. The Λ CDM model is recovered when $\epsilon_{2,0} = 0$, independently of the value of the other parameters; indeed for $\epsilon_{2,0} \rightarrow 0$ we have:

$$\bar{A}(a) \rightarrow 1, \quad \epsilon_2(a) \rightarrow 0, \quad \epsilon_1(a) \rightarrow 0, \quad \forall a, \quad (29)$$

and the kinetic function in Eq. (20) reduces to a cosmological constant.

To produce linear predictions for this theory we use its implementation in the EFTCAMB code, described in Benevento et al. (2019).

3. Theoretical predictions for *Euclid* observables

Both the forecasting method and the tools used in this paper are the same as the ones in EC19 apart from the changes needed to account for the use of MG rather than GR in the predictions of *Euclid* observables. The motivations and the relevant changes in the recipe have been described in a previous paper on forecasts for $f(R)$ theories. We therefore refer the reader to Casas et al. (2023), while here we only remind the reader of the main steps.

3.1. Photometric survey

The observables we consider for the *Euclid* photometric survey are the angular power spectra $C_{ij}^{XY}(\ell)$ between the probe X in the i -th redshift bin, and the probe Y in the j -th bin, where X refers to weak lensing (WL), photometric galaxy clustering (GC_{ph}), or their cross correlation, XC. These are still calculated as in EC19 relying on the Limber approximation and setting to unity the ℓ -dependent factor in the flat sky limit. The spectra are then given by

$$C_{ij}^{XY}(\ell) = c \int_{z_{\min}}^{z_{\max}} dz \frac{W_i^X(z)W_j^Y(z)}{H(z)r^2(z)} P_{\delta\delta}(k_\ell, z), \quad (30)$$

with $k_\ell = (\ell + 1/2)/r(z)$, $r(z)$ the comoving distance to redshift $z = 1/a - 1$, $P_{\delta\delta}(k_\ell, z)$ the nonlinear power spectrum of matter density fluctuations, δ , at wave number k_ℓ and redshift z . We set $(z_{\min}, z_{\max}) = (0.001, 4)$ which span the full range where the source redshift distributions $n_i(z)$ are non vanishing. The GC_{ph} and WL window functions read (Spurio Mancini et al. 2019)

$$W_i^G(k, z) = b_i(k, z) \frac{n_i(z) H(z)}{\bar{n}_i c}, \quad (31)$$

$$W_i^L(k, z) = \frac{3}{2} \Omega_{m,0} \frac{H_0^2}{c^2} (1+z) r(z) \Sigma(z) \int_z^{z_{\max}} dz' \frac{n_i(z') r(z' - z)}{\bar{n}_i r(z')} + W_i^{IA}(k, z), \quad (32)$$

where $n_i(z)/\bar{n}_i$ and $b_i(k, z)$ are, respectively, the normalised galaxy distribution and the galaxy bias in the i -th redshift bin, and $W_i^{IA}(k, z)$ encodes the contribution of intrinsic alignments (IA) to the WL power spectrum. Notice the presence of the function $\Sigma(z)$ in the WL window function which explicitly accounts for the changes in the lensing potential due to the particular MG theory of interest. Its explicit form for the cases under consideration can be found in Section 2. The impact on the background quantities $H(z)$, $r(z)$ and the matter power spectrum $P_{\delta\delta}(k, z)$ are, on the contrary, already taken into account by the dedicated Boltzmann solver so that the GC_{ph} window function remains unchanged.

The IA contribution is computed following the eNLA model adopted in EC19 so that the corresponding window function is

$$W_i^{IA}(k, z) = -\frac{\mathcal{A}_{IA} C_{IA} \Omega_{m,0} \mathcal{F}_{IA}(z) n_i(z) H(z)}{\delta(k, z)/\delta(k, z=0) \bar{n}_i(z) c}, \quad (33)$$

where

$$\mathcal{F}_{IA}(z) = (1+z)^{\eta_{IA}} \left[\frac{\langle L \rangle(z)}{L_\star(z)} \right]^{\beta_{IA}}, \quad (34)$$

with $\langle L \rangle(z)$ and $L_\star(z)$ redshift-dependent mean and the characteristic luminosity of source galaxies as computed from the luminosity function, \mathcal{A}_{IA} , β_{IA} and η_{IA} are the nuisance parameters of the model, and C_{IA} is a constant accounting for dimensional units. This model is the same as the one used in EC19 since IA takes place on astrophysical scales which are unaffected by modifications to gravity. However, MG has an impact on the growth factor introducing a possible scale dependence. This is explicitly taken into account in Eq. (33) through the matter perturbation $\delta(k, z)$, which is considered to be scale dependent in this case. This allows us to consider also the scale dependence introduced by massive neutrinos, which was assumed to be negligible in EC19. We nevertheless stress that, for the models we are considering in this paper, the scale dependence is quite small so that the IA is essentially the same as in the GR case.

3.2. Spectroscopic survey

We now discuss the modelling of the power spectrum to analyse the data from the *Euclid* spectroscopic survey.

For the models considered in this paper, the Compton wavelength of the scalar field is much larger than the scales probed by *Euclid*. Moreover, it is assumed that the speed of propagation of scalar fluctuations is of the order of the speed of light, so that the sound horizon is of the order of the Hubble scale. Under these assumptions, we can apply the quasi-static approximation and relate the scalar field perturbation to the gravitational potential. Since in all these models the weak equivalence principle holds, the modelling of the bias as an expansion in the derivatives of the gravitational potential remains unchanged with respect to the Λ CDM one. To be consistent with the official forecast, we will use the same modelling for galaxy clustering as in EC19.

The observed galaxy power spectrum is given by

$$P_{\text{obs}}(k, \mu_\theta; z) = \frac{1}{q_\perp^2(z) q_\parallel(z)} \left\{ \frac{[b\sigma_8(z) + f\sigma_8(z)\mu_\theta^2]^2}{1 + [f(z)k\mu_\theta\sigma_p(z)]^2} \right\} \times \frac{P_{\text{dw}}(k, \mu_\theta; z)}{\sigma_8^2(z)} F_z(k, \mu_\theta; z) + P_s(z), \quad (35)$$

where $P_{\text{dw}}(k, \mu_\theta; z)$, the de-wiggled power spectrum, includes the correction that accounts for the smearing of the BAO features,

$$P_{\text{dw}}(k, \mu_\theta; z) = P_{\delta\delta}^{\text{lin}}(k; z) e^{-g_\mu k^2} + P_{\text{nw}}(k; z) (1 - e^{-g_\mu k^2}), \quad (36)$$

and $P_{\delta\delta}^{\text{lin}}(k; z)$ stands for the linear matter power spectrum. $P_{\text{nw}}(k; z)$ is a ‘no-wiggle’ power spectrum with the same broadband shape as $P_{\delta\delta}^{\text{lin}}(k; z)$ but without BAO features (see discussion below). The function

$$g_\mu(k, \mu_\theta, z) = \sigma_v^2(z) \left\{ 1 - \mu_\theta^2 + \mu_\theta^2 [1 + f(z)]^2 \right\}, \quad (37)$$

is the nonlinear damping factor of the BAO signal derived by Eisenstein et al. (2007), with

$$\sigma_v^2(z) = \frac{1}{6\pi^2} \int dk P_{\delta\delta}^{\text{lin}}(k, z). \quad (38)$$

The curly bracket in Eq. (35) is the redshift-space-distortion (RSD) contribution correcting for the nonlinear finger-of-God (FoG) effect, where we defined $b\sigma_8(z)$ as the product of the effective scale-independent bias of galaxy samples and the r.m.s. matter density fluctuation $\sigma_8(z)$ (let us note that we marginalize over $b\sigma_8(z)$), while μ_θ is the cosine of the angle θ between the wave vector \mathbf{k} and the line-of-sight direction $\hat{\mathbf{r}}$ and $\sigma_p^2(z) = \sigma_v^2(z)$. Although these parameters are assumed to be the same, they come from two different physical effects, namely large-scale bulk flow for the former and virial motion for the latter.

The factor F_z accounts for the smearing of the galaxy density field along the line-of-sight due to redshift uncertainties. It is given by

$$F_z(k, \mu_\theta; z) = e^{-k^2 \mu_\theta^2 \sigma_\tau^2(z)}, \quad (39)$$

where $\sigma_\tau(z) = c(1+z)\sigma_{0,z}/H(z)$ and $\sigma_{0,z}$ is the error on the measured redshifts.

The factor in front of the curly bracket in Eq. (35) describes the Alcock-Paczynski effect, which is parameterised in terms of

the angular diameter distance $D_A(z)$ and the Hubble parameter $H(z)$ as

$$q_{\perp}(z) = \frac{D_A(z)}{D_{A,\text{ref}}(z)}, \quad (40)$$

$$q_{\parallel}(z) = \frac{H_{\text{ref}}(z)}{H(z)}. \quad (41)$$

Due to the Alcock-Paczynski effect, μ_{θ} and k are re-scaled in a cosmology-dependent way as a function of the projection along and perpendicular to the line-of-sight. In the previous Eq. (35), the arguments μ and k are themselves functions of the “true” $\mu_{\theta,\text{ref}}$ and k_{ref} at the reference cosmology. This relation, which for each argument, is a function of q_{\parallel} and q_{\perp} , can be found in Sect. 3.2.1 of EC19. Finally, the $P_s(z)$ is a scale-independent shot-noise term, which enters as a nuisance parameter (see EC19).

Due to the scale independence of $\sigma_v (= \sigma_p)$, we evaluate it at each redshift bin but we kept it fixed in the Fisher matrix analysis. This method corresponds to the optimistic settings in EC19. We would like to highlight that in this work we take directly the derivatives of the observed galaxy power spectrum with respect to the final parameters, contrary to EC19 where first a Fisher matrix analysis is performed for the redshift dependent parameters $H(z)$, $D_A(z)$ and $f\sigma_8(z)$ and then projected to the final cosmological parameters of interest. However, we checked that both approaches lead to consistent results when considering the Λ CDM and w_0w_a CDM models. The other term appearing in Eq. (36) is the non-wiggle matter power spectrum and this has been obtained applying a Savitzky-Golay filter to the matter power spectrum $P_{\delta\delta}^{\text{lin}}(k, z)$. For more details on this implementation, see EC19.

3.3. Nonlinear modelling for WL

The galaxy power spectrum on mildly nonlinear scales can be modelled by a modified version of the implementation in EC19. This is no more the case when we move to the deeply nonlinear regime where an analytical description of the matter power spectrum is unavailable for the models of our interest.

The wide window functions (in particular, the WL one) entering the prediction of the photometric observables $C_{ij}^{XY}(\ell)$ require an accurate description of nonlinear scales. In particular, one should explicitly account for the impact of baryons, and include nuisance parameters which control the baryonic feedback in order to avoid biasing the parameter estimation (see e.g. Schneider et al. 2020b,a). However, at the moment we do not have accurate *Euclid*-like simulations including baryonic effects, especially in the case of MG cosmologies. Therefore, we ignore these effects in our analysis, leaving their inclusion for a future work. In the following subsections, we comment on the individual prescriptions for each MG model, which will be used to compute the nonlinear matter power spectrum. While having a common prescription at nonlinear scales for all models would be desirable, given the different behaviors of each model at nonlinear scales, this remains an ambitious goal. Currently we have at our disposal codes implementing the specific features of each model which have already been tested and used in literature thus reinforcing the validity of our procedure.

3.3.1. Jordan-Brans-Dicke gravity

For the nonlinear prescription, we use a modified version of HMCODE (Mead et al. 2015, 2016). HMCODE is an augmented halo

model that can be used to make accurate predictions of the nonlinear matter power spectrum over a wide range of cosmologies. A brief summary of how this works is given below.

In the halo model (Cooray & Sheth 2002), the nonlinear matter power spectrum can be written as a sum $P_{\text{NL}}(k, z) = P_{1\text{H}}(k, z) + P_{2\text{H}}(k, z)$ where

$$P_{2\text{H}}(k, z) = P_{\text{lin}}(k, z) \left[\int_0^{\infty} b(M, z) W(M, k, z) n(M, z) dM \right]^2, \quad (42)$$

is the so-called 2-halo term (correlation between different halos) and

$$P_{1\text{H}}(k, z) = \int_0^{\infty} W^2(M, k, z) n(M, z) dM, \quad (43)$$

is the so-called 1-halo term (correlations between mass-elements within each halo). Above M is the halo mass, $P_{\text{lin}}(k, z)$ is the linear matter power spectrum, $n(M, z)$ is the halo mass function and $b(M, z)$ is the linear halo bias.

The window function W is the Fourier transform of the halo matter density profiles:

$$W(M, k, z) = \frac{1}{\bar{\rho}} \int_0^{r_v} 4\pi r^2 \frac{\sin(kr)}{kr} \rho(M, r, z) dr, \quad (44)$$

where $\rho(M, r, z)$ is the radial matter density profile in a host halo of mass M and $\bar{\rho}$ is the mean matter density. The halo mass is related to the virial radius, r_v , via $M = 4\pi r_v^3 \Delta_v(z) \bar{\rho} / 3$, where $\Delta_v(z)$ is the virial halo overdensity. The halo profiles, the halo definition and the halo mass function can either be computed from excursion set models, extracted from numerical simulations and/or parametrised as functions with free parameters which are then fit to data. HMCODE does a combination of this and the resulting fitting function has, for Λ CDM, been shown to be accurate to 2.5% for scales $k < 10 h \text{Mpc}^{-1}$ and redshifts $z < 2$ (Mead et al. 2021).

In Joudaki et al. (2022), a modification of HMCODE that is able to include the effects of JBD, was made using a suite of N -body simulations obtained with modified versions of both the COmoving Lagrangian Acceleration (COLA, Tassev et al. 2013; Winther et al. 2017) and RAMSES (Teyssier 2002) codes. COLA solves for the perturbations around paths predicted from second order Lagrangian perturbation theory (2LPT), and it has proven to be fast and accurate on large scales. This was used for scales $k < 0.5 h \text{Mpc}^{-1}$ to generate a large enough ensemble of simulations and reduce sample variance. On very small scales, up to $k < 10 h \text{Mpc}^{-1}$, RAMSES grid-based hydrodynamical solver with adaptive mesh refinement were used.

The spectra generated by these simulations were then used to calibrate HMCODE. While we do not consider the effects of baryons here, the advantage of HMCODE, rather than Halofit is that the former is able to capture baryonic feedback at $\sim 5\%$ accuracy level up to $k \simeq 10 h \text{Mpc}^{-1}$ (Mead et al. 2021). This will become an important consideration (Schneider et al. 2020b,a) in future, more detailed analyses. To take into account JBD, on top of modifying the expansion history and growth of perturbations, the virialised halo overdensity was modified as

$$\Delta_v = \Omega_m(z)^{-0.352} \times \left\{ d_0 + (418.0 - d_0) \arctan \left[(0.001 |\omega_{\text{BD}} - 50.0|)^{0.2} \right] \frac{2}{\pi} \right\}, \quad (45)$$

where $d_0 = 320.0 + 40.0z^{0.26}$. This modification has the feature that it reduces to the original Λ CDM HMCODE as $\omega_{\text{BD}} \rightarrow \infty$. We stress that this modification is not a physical claim about JBD causing this particular change in the virialised halo overdensity, but rather that this change in the virialised halo overdensity within the HMCODE machinery is able to accurately reproduce the JBD power-spectrum to the given accuracy. The resulting power spectrum with this modification was found to be accurate to 10% for the fitted range $10^4 \gtrsim \omega_{\text{BD}} \geq 50$ and on scales up to $k \simeq 10 h \text{ Mpc}^{-1}$. This nonlinear prescription was made with past weak-lensing surveys in mind and fitted to a range of ω_{BD} and scales that we can realistically constrain at the present time. Let us note that if doing parameter inference with actual *Euclid* data the accuracy here might not be good enough.

We can see in Fig. 1 the comparison of the matter power spectrum and the lensing angular power spectrum of JBD with $\omega_{\text{BD}} = 800$, which we will refer to as JBD1, and their comparison to Λ CDM. In the top left panel we plot the linear (dashed) and nonlinear (solid) matter power spectrum as a function of scale for $z = 0$. In the top right panel we show the ratio of these power spectra with respect to their corresponding Λ CDM cases, using the same σ_8 normalization today.

We can see that for JBD1, the linear power spectrum is almost identical to its standard model counterpart, however the nonlinear power spectrum shows a small suppression on small scales, kicking off at about $k = 0.3 h \text{ Mpc}^{-1}$. It is important to note that, unlike nDGP, the JBD theory is not endowed with gravitational screening so any modification on small scales in the nonlinear power spectrum is inherited from the change in the primordial amplitude, A_s , in the linear power spectrum. In order for σ_8 to be the same in Λ CDM as in JBD we need a higher primordial amplitude A_s . A higher A_s in Λ CDM means nonlinear structures form faster and get more massive, which in the matter power-spectrum then translates into an even higher amplitude on nonlinear scales (i.e. it increases more than linear theory predicts) which gives rise to the small-scale suppression seen in Fig. 1. This effect can also be found in pure Λ CDM if one considers the ratio of the matter power spectrum for two different values of A_s . The result will then be constant on large scales, but shows an enhancement or suppression on small scales. If we instead showed results with the same primordial amplitude in JBD as in Λ CDM then the JBD power-spectrum would show a certain enhancement to Λ CDM on linear scales and an ever bigger enhancement on nonlinear scales, which is more in line with naive expectations of having a larger gravitational constant leading to an enhancement in the matter power-spectrum. The signature we see in the matter power-spectrum naturally impacts the lensing spectrum, which shows a similar suppression at small scales, given that for a given multipole and redshift bin, it is just proportional to the matter power spectrum as defined in Eq. (30).

3.3.2. Dvali-Gabadadze-Porrati gravity

We will model the nonlinear power spectrum using the halo model reaction (Cataneo et al. 2019) which has been shown to agree with N -body simulations at the 2% level down to $k = 3 h \text{ Mpc}^{-1}$ with small variation depending on redshift, degree of modification to GR and mass of neutrinos (Bose et al. 2021). The approach attempts to model nonlinear corrections to the power spectrum coming from modified gravity through the so-called reaction $\mathcal{R}(k, z)$, which employs both 1-loop perturbation theory and the halo model. The nonlinear power spectrum in nDGP is

given by the product

$$P_{\text{NL}}(k, z) = \mathcal{R}(k, z) P_{\text{NL}}^{\text{pseudo}}(k, z), \quad (46)$$

where the *pseudo* power spectrum is a spectrum where all non-linear physics are modelled using GR but the initial conditions are tuned in such a way as to replicate the modified linear clustering at the target redshift. In this work we use the halofit formula of Takahashi et al. (2012) to model $P_{\text{NL}}^{\text{pseudo}}(k, z)$ by supplying the formula with a nDGP input linear matter power spectrum.

The halo model reaction, $\mathcal{R}(k, z)$, is given by a corrected ratio of target-to-pseudo halo model spectra

$$\mathcal{R}(k, z) = \frac{[[1 - \mathcal{E}(z)]e^{-k/k_*(z)} + \mathcal{E}(z)]P_{2\text{H}}(k, z) + P_{1\text{H}}(k, z)}{P_{\text{hm}}^{\text{pseudo}}(k, z)}. \quad (47)$$

The components are given explicitly as

$$P_{\text{hm}}^{\text{pseudo}}(k, z) = P_{2\text{H}}(k, z) + P_{1\text{H}}^{\text{pseudo}}(k, z), \quad (48)$$

$$\mathcal{E}(z) = \lim_{k \rightarrow 0} \frac{P_{1\text{H}}(k, z)}{P_{1\text{H}}^{\text{pseudo}}(k, z)}, \quad (49)$$

$$k_*(z) = -\bar{k} \left\{ \ln \left[\frac{A(\bar{k}, z)}{P_{2\text{H}}(\bar{k}, z)} - \mathcal{E}(z) \right] - \ln [1 - \mathcal{E}(z)] \right\}^{-1}, \quad (50)$$

where

$$A(k, z) = \frac{P_{1\text{-loop}}(k, z) + P_{1\text{H}}(k, z)}{P_{1\text{-loop}}^{\text{pseudo}}(k, z) + P_{1\text{H}}^{\text{pseudo}}(k, z)} P_{\text{hm}}^{\text{pseudo}}(k, z) - P_{1\text{H}}(k, z). \quad (51)$$

$P_{2\text{H}}(k, z)$ is the 2-halo contribution which we can approximate with the (nDGP) linear power spectrum, $P_L(k, z)$ (see for a review on the halo model Cooray & Sheth 2002). $P_{1\text{H}}(k, z)$ and $P_{1\text{H}}^{\text{pseudo}}(k, z)$ are the 1-halo contributions to the power spectrum as predicted by the halo model, with and without modifications to the standard Λ CDM spherical collapse equations, respectively. We remind the reader that by definition, the pseudo cosmology has no nonlinear beyond- Λ CDM modifications. Similarly, $P_{1\text{-loop}}(k, z)$ and $P_{1\text{-loop}}^{\text{pseudo}}(k, z)$ are the 1-loop predictions with and without nonlinear modifications to Λ CDM, respectively. As in previous works, the limit in Eq. (49) is taken to be at $k = 0.01 h \text{ Mpc}^{-1}$ and we compute k_* using $\bar{k} = 0.06 h \text{ Mpc}^{-1}$. This scale is chosen such that the 1-loop predictions are sufficiently accurate at all the redshifts considered.

We note that the correction to the halo model ratio in Eq. (47) has been shown to improve this ratio when there are modifications to gravity that invoke some sort of screening mechanism (Cataneo et al. 2019).

As in previous works, in our halo model calculations we use a Sheth-Tormen mass function (Sheth & Tormen 1999, 2002), a power-law concentration-mass relation (see for example Bullock et al. 2001) and an NFW halo density profile (Navarro et al. 1997). These calculations are performed using the publicly available ReACT code (Bose et al. 2020). We refer the interested reader to this reference for further computational and theoretical details.

Finally, as previously discussed in the JBD case, we show in Fig. (1) the comparison of the matter power spectrum and the lensing angular power spectrum of nDGP vs. Λ CDM as a function of scale for $z = 0$. Here we have chosen for Ω_{rc} the value $\Omega_{\text{rc}} = 0.25$ that is farther away from Λ CDM. We will refer to this

choice as nDGP1 model. The ratio of these power spectra with respect to their corresponding Λ CDM cases has been done using the same σ_8 normalization today. We can see that for nDGP1, the linear matter power spectrum is identical to the Λ CDM one. However, the nonlinear matter power spectrum shows a suppression starting from scales $k = 0.1 h \text{Mpc}^{-1}$, which reaches about 10% at scales of about $k = 1.0 h \text{Mpc}^{-1}$. This impacts of course the lensing spectrum, which shows a similar suppression at small angular scales, given that for a given multipole and redshift bin, it is just proportional to the matter power spectrum as defined in Eq. (30).

As the σ_8 normalization is the same for the Λ CDM reference spectrum, it is essentially the $P_{\text{NL}}^{\text{pseudo}}$ by definition. This means the quantity associated with the green solid curve in the top right panel of Fig. 1 is approximately $\mathcal{R}(k, z = 0)$. This quantity is largely governed by the ratio of the nDGP to pseudo 1-halo terms at $k > 0.1 h \text{Mpc}^{-1}$ (Cataneo et al. 2019). In a nDGP cosmology, there will be more high-mass halos when compared to its GR counterpart due to the supplemental fifth force sourced by the additional degree of freedom. High-mass contributions to the 1-halo term are relatively more suppressed by the NFW density profile (see for example Fig. 9 of Cooray & Sheth 2002, and Eq. 52). This will cause the 1-halo GR power spectrum to be larger than the DGP 1-halo spectrum if the linear clustering in the two cosmologies is the same at the target redshift.

We note that if instead we fix the same primordial amplitude of perturbations, we will have the reverse, more halos will have formed by the target redshift in the nDGP cosmology giving an enhancement of the 1-halo term over GR. We refer the reader to Figs. 6 and 8 in Cataneo et al. (2019) highlighting these two scenarios, GR and nDGP with the same late time amplitude of linear perturbations and one with the same early time amplitude respectively.

3.3.3. k -mouflage gravity

For the KM nonlinear matter power spectrum, we use a similar analytical approach that combines 1-loop perturbation theory with a halo model. This method was introduced in Valageas et al. (2013) for the standard Λ CDM cosmology. As in usual halo models, it splits the matter power spectrum over 2-halo and 1-halo contributions, as in Eq. (48), but it uses a Lagrangian framework to evaluate these two contributions in terms of the pair-separation probability distribution. This provides a Lagrangian-space regularisation of perturbation theory, which matches standard perturbation theory up to 1-loop order and includes a partial resummation of higher-order terms, such that the pair-separation probability distribution is positive and normalised to unity at all scales. Thus, the two-halo term goes beyond the Zeldovich approximation by including a non-zero skewness, which enables the consistency with standard perturbation theory up to 1-loop order, as well as a simple Ansatz for higher-order cumulants inspired by the adhesion model. The 1-halo term includes a counter-term that ensures its falloff at low k , in agreement with the conservation of matter and momentum,

$$P_{1\text{H}}(k) = \int_0^\infty \frac{dv}{v} f(v) \frac{M}{\bar{\rho}(2\pi)^3} \left[\tilde{u}_M(k) - \tilde{W}(kq_M) \right]^2, \quad (52)$$

where $\tilde{u}_M(k)$ is the normalised Fourier transform of the halo radial profile, $\tilde{W}(kq_M)$ is the normalised Fourier transform of the top-hat of Lagrangian radius q_M , and $f(v)$ is the normalised halo mass function. This counterterm is not introduced by hand, as it arises directly from the splitting of the matter power spectrum

over 2-halo and 1-halo contributions within a Lagrangian framework, which by construction satisfies the conservation of matter. Additionally, v is defined as $\delta_c/\sigma(M)$, where δ_c is the linear density contrast associated to a nonlinear density contrast of 200, and $\sigma(M)$ is the root mean square of the linear density contrast at mass scale M . The threshold δ_c is sensitive to the modification of gravity. In principles it also depends on M , as the shells in the spherical collapse are coupled and evolve differently depending on their masses due to nonlinear screening. However, for the models that we consider here, screening is negligible beyond $1 h^{-1} \text{Mpc}$ (clusters are not screened), so that δ_c is independent of M .

This nonlinear modelling was extended in Brax & Valageas (2013) to several modified-gravity scenarios ($f(R)$ theories, dilaton and symmetron models), and in Brax & Valageas (2014); Brax et al. (2015) to KM models. This involves the computation of the impact of modified gravity on both the linear and 1-loop contributions to the matter power spectrum, which enter the 2-halo term, and on the spherical collapse dynamics, which enter the 1-halo term through the halo mass function. Therefore, this nonlinear modelling exactly captures the modification of gravity both up to 1-loop order and at the level of the fully nonlinear spherical collapse. The Ansatz for the partial resummation of higher-order terms is the same as for the standard Λ CDM cosmology (this implies that their values are also modified as they depend on the lower orders to ensure the positivity and the normalisation of the underlying pair distribution). A comparison with numerical simulations (Brax & Valageas 2013) for $f(R)$ theories (with $|f_{R_0}| = 10^{-4}, 10^{-5}$ and 10^{-6}), shows that this approach captures the relative deviation from the Λ CDM power spectrum at $z = 0$ up to $k = 3 h \text{Mpc}^{-1}$. We have not compared this recipe with numerical simulations of the KM theories yet, which have only recently been performed (Hernández-Aguayo et al. 2022). However, we expect at least the same level of agreement, as the KM models are simpler and closer to the Λ CDM cosmology than the $f(R)$ models (as in Λ CDM, the linear growth rate is scale independent).

We can see in Fig. 1 the comparison between the KM1 model defined with $\epsilon_{2,0} = -0.04$ and its Λ CDM counterpart, normalised to the same σ_8 and cosmological parameters at $z = 0$, for the matter and cosmic shear power spectra. We can notice that the ratio of the linear matter power spectra increases on intermediate scales ($10^{-2} < k < 1 h \text{Mpc}^{-1}$): this is due to the change of the background evolution, which slightly affects the scales at matter-radiation equality. Indeed, $H(z)$ is greater for KM1 at high redshift (Benevento et al. 2019), which implies a smaller Hubble radius at matter-radiation equality. This in turns means that the change of the slope of the linear power spectrum, from $P_L(k) \sim k^{n_s}$ to $P_L(k) \propto k^{n_s-4}$, is shifted to smaller scales, and whence to higher k . This implies that the ratio $P_{\text{KM1}}^{\text{mm}}/P_{\text{ACDM}}^{\text{mm}}$ grows on these intermediate scales, where the linear power spectrum changes slope, because of this delay to higher k of the transition. Because the two spectra have the same σ_8 and the ratio $P_{\text{KM1}}^{\text{mm}}/P_{\text{ACDM}}^{\text{mm}}$ grows with k , the ratio is below unity at low k and above unity at high k . Moreover the linear growth rates are scale-independent for both KM and Λ CDM, therefore the ratio $P_{\text{KM1}}^{\text{mm}}/P_{\text{ACDM}}^{\text{mm}}$ goes to a constant at very low k and at very high k , where the slopes of both linear power spectra are equal to n_s or $n_s - 4$ (i.e., outside of the intermediate scales where the slope of the linear power spectrum slowly runs with k). This flat ratio can be clearly seen in Fig. 1 at low k . The amplitude of the deviation is set by the parameter $\epsilon_{2,0}$. There is a significant multiplicative factor, of about 7, as it reaches 30% for $\epsilon_{2,0} = -0.04$. This is partly due to nonlinear effects in the scalar field sector,

both in the background and in the linear growth rate, which are not completely irrelevant. At $z = 0$, even though $\epsilon_2 = -0.04$ we have $\epsilon_1 \simeq 0.12$, whereas at linear order in the scalar field dynamics we should have expected that $\epsilon_1 = -\epsilon_2$. As the growth of structures is actually sensitive to ϵ_1 , this leads to a stronger effect than could be expected from the value of ϵ_2 itself. Then, the power spectrum being a quadratic functional of the density field gives an additional amplification factor of 2 for relative perturbations.

Beyond this global behavior of the ratio $P_{\text{KM1}}^{\text{mm}}/P_{\Lambda\text{CDM}}^{\text{mm}}$, another impact of the slight modification of the background is to shift the baryon acoustic oscillations. This leads to the oscillations seen at BAO scales, $k \sim 0.01 h \text{Mpc}^{-1}$. Nonlinear effects lead to a decrease of the ratio $P_{\text{KM1}}^{\text{mm}}/P_{\Lambda\text{CDM}}^{\text{mm}}$ as compared with the linear prediction of mildly nonlinear scales. This is due to the loss of information in the power spectrum in the nonlinear regime, which can be related to the universal NFW profile of virialized halos within the halo model. Then, the shape of the nonlinear power spectrum at those scales is mostly set by the scale where the nonlinear transition takes place and this happens to occur at somewhat larger scales for the ΛCDM counterpart (i.e. the higher linear power at higher k in the KM1 scenario is mostly erased by the nonlinear dynamics).

As usual, the integration along the line of sight leads to a much smoother curve for the cosmic shear angular power spectrum. Even though the 3D nonlinear matter power spectrum is reduced at $z = 0$ for KM1 as compared with ΛCDM , as seen in the upper right panel, the lensing power is increased, as seen in the lower right panel. This is due to the coupling function $A(\varphi)$, which is greater than unity at $z > 0$ and leads to a higher value of the phenomenological function Σ , see Eq. (24), or in other words to a greater Newton constant at high redshift.

4. Survey specifications and analysis method

We will vary as base cosmological parameters:

$$\Theta = \{\Omega_{\text{m},0}, \Omega_{\text{b},0}, h, n_s, \sigma_8\}, \quad (53)$$

for which we choose the following fiducial values:

$$\begin{aligned} \Omega_{\text{m},0} &= 0.315, & \Omega_{\text{b},0} &= 0.049, \\ h &= 0.6737, & n_s &= 0.966, \end{aligned} \quad (54)$$

where $\Omega_{\text{m},0} = \Omega_{\text{c},0} + \Omega_{\text{b},0} + \Omega_{\nu,0}$. To fix the fiducial value for σ_8 we will use the same initial amplitude of primordial perturbations for all models, namely $A_s = 2.09681 \times 10^{-9}$. Note that the fiducial cosmology includes massive neutrinos with total mass of $\Sigma m_\nu = 0.06 \text{eV}$, but we keep Σm_ν fixed in the following Fisher matrix analysis. In the following we will specify the σ_8 value for each model along with the fiducial values of the model parameters:

1. JBD

$$\begin{aligned} \Theta_{\text{fid},1} &= \{\sigma_8 = 0.816, \log_{10} \omega_{\text{BD}} = 2.90309\} \quad (\text{JBD1}); \\ \Theta_{\text{fid},2} &= \{\sigma_8 = 0.812, \log_{10} \omega_{\text{BD}} = 3.39794\} \quad (\text{JBD2}). \end{aligned} \quad (55)$$

These values correspond to $\omega_{\text{BD}} = 800$ and $\omega_{\text{BD}} = 2500$ respectively. In these cases the initial value of the scalar field has been fixed to $\phi_{\text{ini}} = 1/G_{\text{N}}$.

2. nDGP

$$\begin{aligned} \Theta_{\text{fid},1} &= \{\sigma_8 = 0.8690, \log_{10} \Omega_{\text{rc}} = -0.60206\} \quad (\text{nDGP1}); \\ \Theta_{\text{fid},2} &= \{\sigma_8 = 0.8105, \log_{10} \Omega_{\text{rc}} = -6\} \quad (\text{nDGP2}). \end{aligned} \quad (56)$$

These values correspond to $\Omega_{\text{rc}} = 0.25$ and $\Omega_{\text{rc}} = 10^{-6}$, respectively for nDGP1 and nDGP2.

3. KM

$$\begin{aligned} \Theta_{\text{fid},1} &= \{\sigma_8 = 0.994, \epsilon_2 = -0.04\} \quad (\text{KM1}); \\ \Theta_{\text{fid},2} &= \{\sigma_8 = 0.813, \epsilon_2 = -0.0001\} \quad (\text{KM2}). \end{aligned} \quad (57)$$

We follow EC19 for setting up the specifics of the photometric probes as we briefly summarise here. The sources are split in 10 equi-populated redshift bins whose limits are obtained from the redshift distribution

$$n(z) \propto \left(\frac{z}{z_0}\right)^2 \exp\left[-\left(\frac{z}{z_0}\right)^{3/2}\right], \quad (58)$$

with $z_0 = 0.9/\sqrt{2}$ and the normalisation set by the requirement that the surface density of galaxies is $\bar{n}_g = 30 \text{arcmin}^{-2}$. This is then convolved with the sum of two Gaussians to account for the effect of photometric redshift. Galaxy bias is assumed constant within each redshift bin, with fiducial values $b_i = \sqrt{1 + \bar{z}_i}$, and \bar{z}_i the bin centre. Any possible scale dependence of the bias introduced by GR is taken to be negligible.

As in EC19, we consider a Gaussian only covariance whose elements are given by

$$\begin{aligned} \text{Cov}\left[C_{ij}^{\text{AB}}(\ell), C_{kl}^{\text{CD}}(\ell')\right] &= \frac{\delta_{\ell\ell'}^{\text{K}}}{(2\ell + 1)f_{\text{sky}}\Delta\ell} \\ &\times \left\{ \left[C_{ik}^{\text{AC}}(\ell) + N_{ik}^{\text{AC}}(\ell) \right] \left[C_{jl}^{\text{BD}}(\ell') + N_{jl}^{\text{BD}}(\ell') \right] \right. \\ &\quad \left. + \left[C_{il}^{\text{AD}}(\ell) + N_{il}^{\text{AD}}(\ell) \right] \left[C_{jk}^{\text{BC}}(\ell') + N_{jk}^{\text{BC}}(\ell') \right] \right\}, \end{aligned} \quad (59)$$

where upper-case (lower-case) Latin indexes run over WL, GC_{ph} (all tomographic bins), $\delta_{\ell\ell'}^{\text{K}}$ is the Kronecker delta symbol coming from the lack of correlation between different multipoles (ℓ, ℓ'), $f_{\text{sky}} \simeq 0.36$ is the survey sky fraction, and $\Delta\ell$ denotes the width of the 100 logarithmic equi-spaced multipole bins. Note that, for the observables of interest here, we can take a white noise so that it is

$$N_{ij}^{\text{LL}}(\ell) = \frac{\delta_{ij}^{\text{K}}}{\bar{n}_i} \sigma_\epsilon^2, \quad (60)$$

$$N_{ij}^{\text{GG}}(\ell) = \frac{\delta_{ij}^{\text{K}}}{\bar{n}_i}, \quad (61)$$

$$N_{ij}^{\text{GL}}(\ell) = 0, \quad (62)$$

where $\sigma_\epsilon^2 = 0.3^2$ is the variance of observed ellipticities.

We keep following EC19 for evaluating the Fisher matrix $F_{\alpha\beta}(z_i)$ for the observed galaxy power spectrum. Here, α and β run over the cosmological parameters of the set Θ , the index i labels the redshift bin, each respectively centred in $z_i = \{1.0, 1.2, 1.4, 1.65\}$, whose widths are $\Delta z = 0.2$ for the first three bins and $\Delta z = 0.3$ for the last bin. As a difference with respect to EC19, we adopt here the direct derivative approach varying the observed galaxy power spectrum with respect to the cosmological parameters directly. We include two additional redshift-dependent parameters $\ln b\sigma_8(z_i)$ and $P_s(z_i)$ that we marginalise over. Spectroscopic galaxy bias, $b(z)$, and expected number density of H α emitters, $n(z)$, are as reported in Table 3 of EC19.

For all probes, we consider an optimistic and a pessimistic scenario defined according to the specifications for WL, GC_{ph} and GC_{sp} in Table 1. Note that, for GC_{sp}, we have added a third

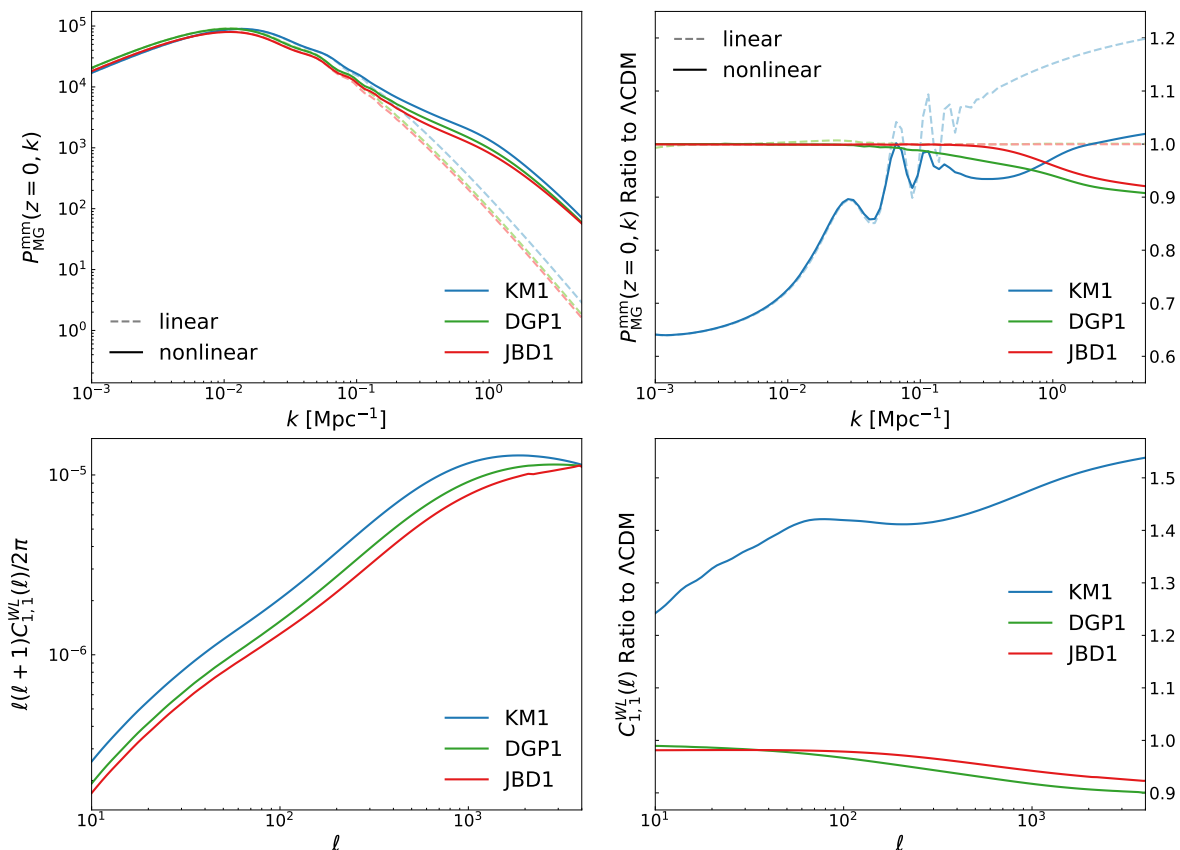


Fig. 1. Large-scale structure observables for the different MG models considered in this work evaluated at the fiducial values of the model parameters used for the Fisher matrix analysis. **Top Left:** The linear (dashed) and nonlinear (solid lines) matter power spectrum $P_{\delta\delta}(z, k)$ entering Eqs. (36) and (30), respectively, evaluated at redshift $z = 0$, for KM1 ($\epsilon_{2,0} = -0.04$, blue), JBD1 ($\omega_{\text{BD}} = 800$, red) and nDGP1 ($\Omega_{\text{rc}} = 0.25$, green). **Top Right:** Ratio of the matter power spectra for the above mentioned models with respect to their ΛCDM counterpart with the same value of σ_8 today, both for the linear (dashed) and nonlinear (solid) cases. While for nDGP1 and JBD1 the linear ratio remains constant, in the case of KM1 the ratio shows large-scale damping and oscillatory features that appear at scales around $k \approx 0.1 h \text{ Mpc}^{-1}$. **Bottom Left:** Cosmic shear (WL) angular power spectra for the first bin $i = j = 1$, defined in Eq. (30) for the three models considered above, with the same legend labels. **Bottom Right:** Ratio of the cosmic shear $C_{i,j}(\ell)$ to their ΛCDM counterpart, for the bin combination $i = j = 1$. For JBD1 and nDGP1 the suppression in the nonlinear power spectrum can also be seen as a suppression of the lensing angular spectra. For KM1, however, although the nonlinear power spectrum is also decreased at small scales the lensing enhancement function Σ defined in Eq. (24) is larger than 1 at $z > 0$, giving an overall increase in the lensing $C_{i,j}(\ell)$ when compared to ΛCDM .

scenario, referred to as *quasi-linear*, fixing the maximum wavenumber to $k_{\text{max}} = 0.15 h \text{ Mpc}^{-1}$. We explore this more conservative case since the underlying matter power spectrum of Eq. (36) that we are using in our observed galaxy power spectrum recipe is a linear one. Nonlinear corrections actually start playing a role for wavenumbers larger than $k = 0.1 h \text{ Mpc}^{-1}$ for the redshifts in consideration (see Taruya et al. 2010). Cutting at a lower k_{max} should avoid any bias induced by neglecting nonlinear corrections below this scale. However, such a severe cut also removes part of the information encoded in GC_{sp} so that we want to quantify how this affects the constraints. In all scenarios, we fix the $\sigma_{\text{v}} = \sigma_{\text{p}}$ nuisance parameter for GC_{sp} to the values directly calculated from Eq. (38) for the fiducial cosmological parameters.

We consider both GC_{sp} alone and the combination of all photometric probes: GC_{ph} , WL, and their XC. Moreover, we also consider the full combination of all *Euclid* main probes: GC_{sp} , GC_{ph} , WL, and the XC between GC_{ph} and WL. It is important to mention that we account for all the mixed terms in the covariance matrix for the photometric probes such as, for instance, $\text{Cov}[C_{ij}^{\text{LL}}(\ell), C_{kl}^{\text{GL}}(\ell)]$. However, we follow EC19 in neglecting any correlation between GC_{sp} and the photometric probes. In the pessimistic scenario, we further impose a cut $z < 0.9$ to GC_{ph} and

XC to remove any overlap between these probes and GC_{sp} . Note that such a cut is applied only when we add GC_{sp} to the photometric probes, while it is not when using photometric probes alone in the pessimistic case. No cut is ever applied in the optimistic case.

5. Results

In this section we discuss the results of the Fisher matrix analysis for the three models under investigation, JBD, nDGP and KM, and for each of them we consider two fiducial cases presented in Sect. 4. Additionally, for each case we consider a quasi-linear, pessimistic and optimistic scenario as discussed in Sect. 4. In the following we present the 68.3% and 95.4% joint marginal error contours on the cosmological and model parameters for the optimistic setting and for completeness we include the contour plots for the pessimistic scenario in the Appendix A. We stress that we are interested in detecting a non zero value for the model's parameters, therefore we present the relative errors on the corresponding fiducial values. In the specific cases of JBD and nDGP we performed the Fisher analysis on the logarithm of the extra parameter, namely $\log_{10} X$ with $X = \omega_{\text{BD}}$ and $X = \Omega_{\text{rc}}$ for JBD

Table 1. *Euclid* survey specifications for WL, GC_{ph} and GC_{sp}.

Survey area	A_{survey}	15 000 deg ²
WL		
Number of photo- z bins	N_z	10
Galaxy number density	\bar{n}_{gal}	30 arcmin ⁻²
Intrinsic ellipticity dispersion	σ_ϵ	0.30
Minimum multipole	ℓ_{min}	10
Maximum multipole	ℓ_{max}	
– Pessimistic		1500
– Optimistic		5000
GC _{ph}		
Number of photo- z bins	N_z	10
Galaxy number density	\bar{n}_{gal}	30 arcmin ⁻²
Minimum multipole	ℓ_{min}	10
Maximum multipole	ℓ_{max}	
– Pessimistic		750
– Optimistic		3000
GC _{sp}		
Number of spectro- z bins	n_z	4
Centres of the bins	z_i	{1.0, 1.2, 1.4, 1.65}
Error on redshift	$\sigma_{0,z}$	0.001
Minimum scale	k_{min}	0.001 h Mpc ⁻¹
Maximum scale	k_{max}	
– Quasi-linear		0.15 h Mpc ⁻¹
– Pessimistic		0.25 h Mpc ⁻¹
– Optimistic		0.30 h Mpc ⁻¹

and nDGP respectively. This choice is dictated by the fact that we cannot perform a Fisher analysis on a parameter varying by order of magnitudes. Additionally, we need to use as parameter a quantity that is of order one in the analysis in order to avoid having large differences between the largest and lowest eigenvalues of the Fisher matrix. For the specific case of nDGP, the use of the logarithm of the model's parameter allows us to consider only its positive viable range, which would not be possible if we performed a Fisher analysis directly on Ω_{rc} . We note indeed that a prior like $\Omega_{\text{rc}} > 0$ cannot be imposed a priori in the Fisher analysis. Beside discussing the results on $\log_{10} X$ we will also report on the uncertainties on the parameter itself, X . We note that we cannot use a Jacobian transformation to convert between the Fisher matrices because the transformation between the two parameterisations is nonlinear and the assumption of Gaussianity is valid for the logarithmic parameterisation only. In order to obtain the constraints on the parameter X we use:

$$X^{(\pm)} = X_{\text{fid}} \times 10^{\pm\sigma_{\log_{10} X}}. \quad (63)$$

As a consequence the uncertainties on X will be asymmetrical. We now proceed to discuss in detail each model.

In order to have a global view on the results for the three MG models analysed, we summarise in Fig. 2 the 68.3% marginal errors on the models parameters, $\log_{10} \omega_{\text{BD}}$ for JBD, $\log_{10} \Omega_{\text{rc}}$ for nDGP and $\epsilon_{2,0}$ for KM in all the scenarios and combinations of probes we used. Let us note that we did not consider WL probe alone because we verified that WL provides constraints roughly of the same order as the GC_{sp} ones. When we combine with GC_{ph} and XC the constraints are significantly boosted. Additionally, we note that the constraining power of the spectroscopic sample is very weak and this is due to the fact that we do not go deep enough in the nonlinear regime and also because when using GC probes we introduce degeneracies among the

MG parameters, amplitudes and bias parameters. These features characterise all the models.

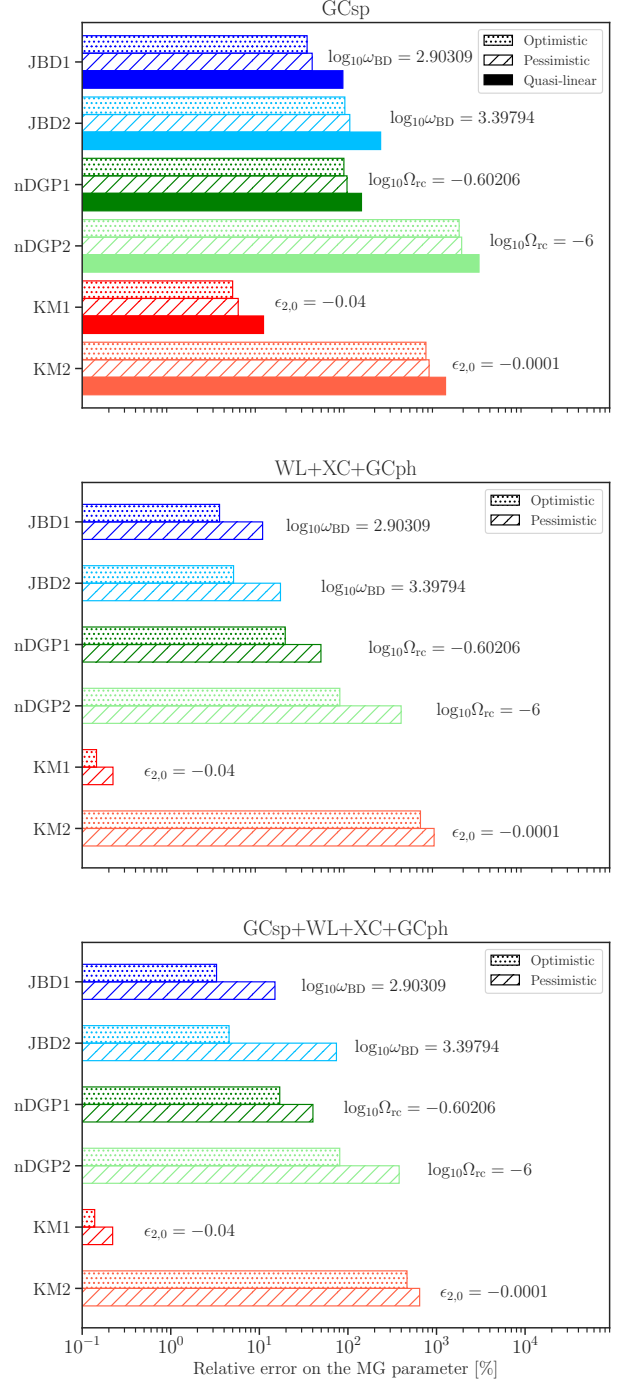


Fig. 2. Marginalised 1σ errors on the models' parameters relative to their corresponding fiducial values, for JBD (case 1 in blue and case 2 in cyan), nDGP (case 1 in green and case 2 in light green) and KM (case 1 in red and case 2 in light red). We show the marginalised 1σ errors for GC_{sp} in the optimistic (dotted area), pessimistic (dashed area) and quasi-linear (filled area) scenarios (top panel), for WL+XC+GC_{ph} in the optimistic and pessimistic cases (central panel) and for the GC_{sp}+WL+XC+GC_{ph} in the optimistic and pessimistic cases.

5.1. Jordan-Brans-Dicke gravity

There are remarkably strong non-cosmological constraints on JBD gravity, with current bounds of order $\omega_{\text{BD}} > 10^5$. But, as pointed out above, it is useful to look at JBD gravity as a long wavelength limit of more general scalar-tensor theories with a wide range of small scale limits which may be endowed with gravitational screening. It then makes sense to focus on what we already know from cosmology, where constraints are of order $\omega_{\text{BD}} > 10^3$, independently from what we know from non-cosmological systems. Two further, practical reasons lead us to choose $\omega_{\text{BD}} \sim 10^3$. First of all this value is at limits of the range for which we have calibrated the nonlinear prescription we are using. Second, the likelihood is very flat for high values of ω_{BD} which can lead to numerical errors in the finite differences of the Fisher matrix evaluation for some of the observables. We thus consider two cases for JBD. The first fiducial with $\omega_{\text{BD}} = 800$ (JBD1) and the second one with $\omega_{\text{BD}} = 2500$ (JBD2). Whereas the first one is nearly compatible with the most recent constraints from publicly available CMB and LSS data, the second one is well within the current bounds (Ballardini et al. 2020; Joudaki et al. 2022; Ballardini et al. 2022). Table 2 summarises the relative (with respect to the fiducial values) uncertainties for the cosmological and model parameters in the quasi-linear, pessimistic and optimistic *Euclid* cases. Fig. 3 shows the 68.3% and 95.4% joint marginal error contours on the cosmological model parameters for the optimistic settings for both JBD1 (left panel) and JBD2 (right panel). Note that as in Casas et al. (2023) for $f(R)$, we have performed the Fisher matrix analysis on the parameter $\log_{10} \omega_{\text{BD}}$, instead of directly on ω_{BD} , since for large numbers and differences in the order of magnitude, the Fisher matrix derivatives might become unstable.

In the optimistic setting, we find that *Euclid* will be able to constrain $\log_{10} \omega_{\text{BD}}$ as follows:

- JBD1:
 - at 35% for the GC_{sp} alone;
 - at 3.6% when considering the combination $\text{WL}+\text{XC}+\text{GC}_{\text{ph}}$;
 - at 3.3% for $\text{GC}_{\text{sp}}+\text{WL}+\text{XC}+\text{GC}_{\text{ph}}$.
- JBD2:
 - at 92% for the GC_{sp} alone;
 - at 5.1% when considering the combination $\text{WL}+\text{XC}+\text{GC}_{\text{ph}}$;
 - at 4.6% for $\text{GC}_{\text{sp}}+\text{WL}+\text{XC}+\text{GC}_{\text{ph}}$.

For JBD1 the parameter $\log_{10} \omega_{\text{BD}}$ can be measured at high statistical significance even in the pessimistic case, whereas this does not hold for JBD2.

We now discuss the forecast errors on the parameter ω_{BD} propagating the uncertainties according to Eq. (63). For JBD1 we obtain $\omega_{\text{BD}} = 800^{+8000}_{-730}$ for GC_{sp} , $\omega_{\text{BD}} = 800^{+210}_{-170}$ for $\text{WL}+\text{XC}+\text{GC}_{\text{ph}}$ and $\omega_{\text{BD}} = 800^{+200}_{-160}$ for $\text{GC}_{\text{sp}}+\text{WL}+\text{XC}+\text{GC}_{\text{ph}}$; these results correspond to relative errors of 1000%, 27% and 25%, respectively. For JBD2, always in the case of optimistic settings, we obtain $\omega_{\text{BD}} = 2500^{+1200}_{-820}$ for $\text{WL}+\text{XC}+\text{GC}_{\text{ph}}$ and $\omega_{\text{BD}} = 2500^{+1070}_{-750}$ for $\text{GC}_{\text{sp}}+\text{WL}+\text{XC}+\text{GC}_{\text{ph}}$; these correspond to relative errors of 48% and 40%, respectively (JBD2 is unconstrained by GC alone).

These results for the optimistic settings demonstrate how *Euclid* alone could potentially detect at statistically significant level values of ω_{BD} which are compatible with current publicly available CMB and LSS data (Ballardini et al. 2020; Joudaki et al. 2022; Ballardini et al. 2022), but not those which are compatible with Solar System constraints. Although *Euclid* specifications

are not exactly the same, these results we find here are consistent with previous ones in Ballardini et al. (2019), once rewritten in the coupling to the curvature $\gamma = (4\omega_{\text{BD}})^{-1}$.

Finally, let us note that in the pessimistic setting we find that, for some parameters, the combination of the photometric probes has more power in constraining than the full combination with spectroscopic probes, see Table 2 and Fig. A.1. This is because for the pessimistic setting we adopt a cut in redshift as described in Sect. 4 to avoid possible overlaps in z . Therefore, we lose the power from GC_{ph} at high redshift. This contingency is present only for the JBD case and not for the other models we study in this work. We identify the physical mechanism behind it in the fact that JBD does not have a proper screening mechanism, while, on the contrary, nDGP and KM include it such that at non-linear scales they recover ΛCDM . This reduces the importance of the constraining power coming from nonlinearities (which is captured by photometric probes) for the latter models, being instead important for the former. We show further results in Appendix A where we present the results without this z -cut.

5.2. Dvali-Gabadadze-Porrati gravity

The two cases considered for the nDGP model are $\log_{10} \Omega_{\text{rc}} = -0.60206$ (nDGP1) and $\log_{10} \Omega_{\text{rc}} = -6$ (nDGP2). We summarise the 68.3% marginalised errors (relative to the fiducial values) in Table 3 on the cosmological and model parameters in the optimistic, pessimistic and quasi-linear case. We show in Fig. 4 the 68.3% and 95.4% joint marginal error contours on cosmological and model parameters for the optimistic scenario for both nDGP1 (left panel) and nDGP2 (right panel). In Fig. A.2 we show the same but for the pessimistic setting.

In the optimistic setting, we find that *Euclid* will be able to constrain $\log_{10} \Omega_{\text{rc}}$ as follows:

- nDGP1:
 - at 90% for GC_{sp} alone;
 - at 20% when considering $\text{WL}+\text{XC}+\text{GC}_{\text{ph}}$;
 - at 17% for $\text{GC}_{\text{sp}}+\text{WL}+\text{XC}+\text{GC}_{\text{ph}}$.
- nDGP2:
 - GC_{sp} has no power in constraining the parameter.
 - at 81% for both $\text{WL}+\text{XC}+\text{GC}_{\text{ph}}$ and $\text{GC}_{\text{sp}}+\text{WL}+\text{XC}+\text{GC}_{\text{ph}}$.

Regardless of the specific case considered (nDGP1 or nDGP2), the power in constraining $\Omega_{\text{m},0}$, $\Omega_{\text{b},0}$ and h is the same, while n_s and σ_8 are better constrained in the nDGP2 case. For example, in the optimistic setting, n_s for $\text{WL}+\text{XC}+\text{GC}_{\text{ph}}$ is constrained at 0.52% for nDGP1 and 0.37% for nDGP2 and they further improve when considering the full combination of probes, being, respectively, 0.37% and 0.17%. In Fig. 4, in the $\log_{10} \Omega_{\text{rc}} - n_s$ panel, we notice that the two parameters are anti-correlated in the nDGP1 case. This makes the forecast errors on n_s larger than the nDGP2 case where the anti-correlation disappears. A similar discussion can be done for the σ_8 parameter. Indeed, in the optimistic setting, for nDGP1 we have 0.37% for $\text{WL}+\text{XC}+\text{GC}_{\text{ph}}$ and 0.26% for the full combination of probes, while for the nDGP2 model we obtain 0.25% and 0.14%, respectively.

As previously done for the JBD model, we translate the forecast errors on the parameter $\log_{10} \Omega_{\text{rc}}$ to the parameter Ω_{rc} , see Eq. (63). Quantitatively for the optimistic scenario, for nDGP1 we get $\Omega_{\text{rc}} = 0.25^{+0.62}_{-0.18}$ for GC_{sp} , $\Omega_{\text{rc}} = 0.25^{+0.08}_{-0.06}$ for $\text{WL}+\text{XC}+\text{GC}_{\text{ph}}$ and $\Omega_{\text{rc}} = 0.25^{+0.07}_{-0.05}$ for $\text{GC}_{\text{sp}}+\text{WL}+\text{XC}+\text{GC}_{\text{ph}}$. These correspond to relative errors that can reach 247%, 32% and 26% respectively. For nDGP2 we obtain an upper bound

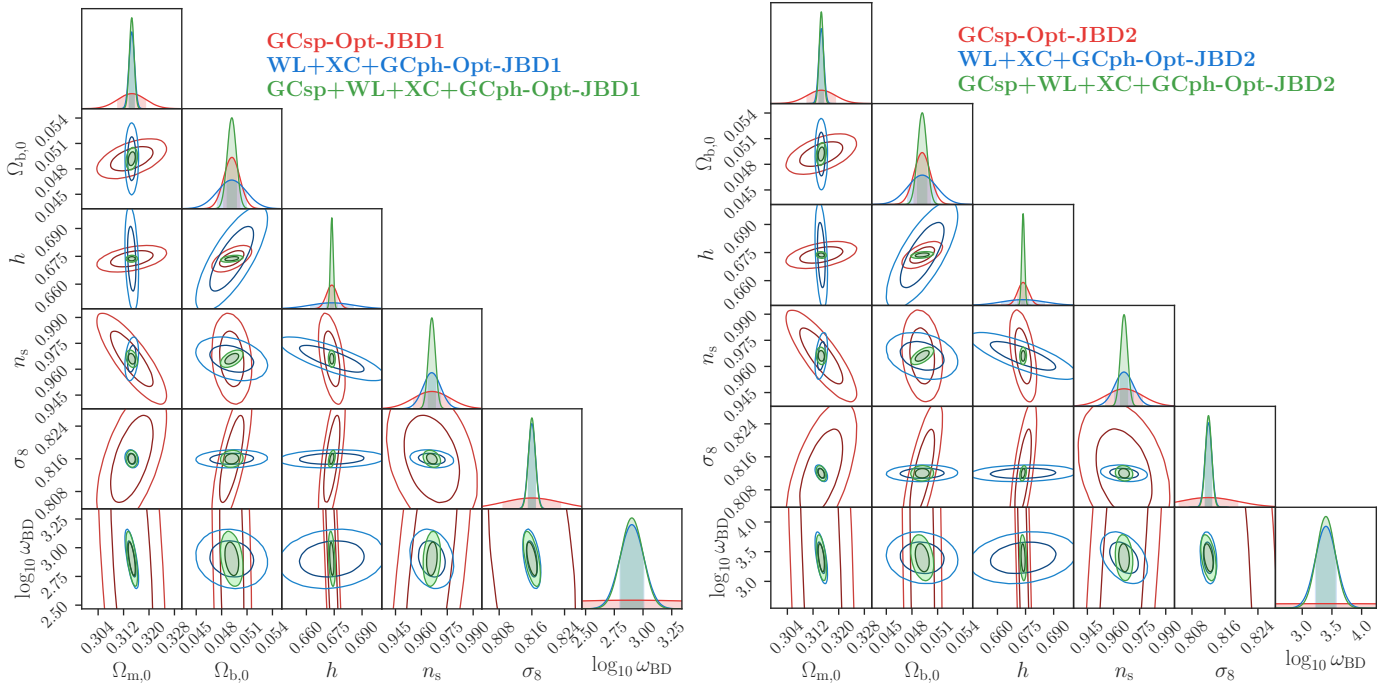


Fig. 3. 68.3% and 95.4% joint marginal error contours on the cosmological parameters for JBD1 (left panel) and JBD2 (right panel) in the optimistic case. In red GC_{sp} , in blue $WL+XC+GC_{ph}$ and in green $GC_{sp}+WL+XC+GC_{ph}$.

Table 2. Forecast 1σ marginal errors on the cosmological and model parameters, relative to their corresponding fiducial value, for JBD1 and JBD2 in the pessimistic, quasi-linear and optimistic cases, using *Euclid* observations GC_{sp} , $WL+XC+GC_{ph}$ and $GC_{sp}+WL+XC+GC_{ph}$.

JBD1 $\omega_{BD} = 800$						
	$\Omega_{m,0}$	$\Omega_{b,0}$	$\log_{10} \omega_{BD}$	h	n_s	σ_8
Pessimistic setting						
GC_{sp} ($k_{max} = 0.15 h \text{ Mpc}^{-1}$) (quasi-linear)	3.87%	6.68%	87.72%	1.52%	2.46%	1.95%
GC_{sp} ($k_{max} = 0.25 h \text{ Mpc}^{-1}$)	1.59%	2.35%	39.49%	0.53%	1.24%	0.98%
$WL+XC+GC_{ph}$	0.37%	5.10%	10.89%	3.20%	1.25%	0.34%
$GC_{sp}+WL+XC+GC_{ph}$	0.55%	1.44%	15.01%	0.27%	0.52%	0.43%
Optimistic setting						
GC_{sp} ($k_{max} = 0.3 h \text{ Mpc}^{-1}$)	1.39%	1.91%	34.60%	0.42%	1.09%	0.85%
$WL+XC+GC_{ph}$	0.27%	3.43%	3.55%	1.69%	0.52%	0.11%
$GC_{sp}+WL+XC+GC_{ph}$	0.23%	1.08%	3.29%	0.11%	0.21%	0.10%
JBD2 $\omega_{BD} = 2500$						
Pessimistic setting						
GC_{sp} ($k_{max} = 0.15 h \text{ Mpc}^{-1}$) (quasi-linear)	3.88%	6.74%	233.99%	1.53%	2.45%	2.01%
GC_{sp} ($k_{max} = 0.25 h \text{ Mpc}^{-1}$)	1.59%	2.36%	104.99%	0.53%	1.24%	0.99%
$WL+XC+GC_{ph}$	0.34%	5.09%	17.32%	3.21%	1.24%	0.27%
$GC_{sp}+WL+XC+GC_{ph}$	1.42%	1.96%	74.17%	0.47%	1.01%	0.97%
Optimistic setting						
GC_{sp} ($k_{max} = 0.3 h \text{ Mpc}^{-1}$)	1.39%	1.92%	92.30%	0.43%	1.09%	0.87%
$WL+XC+GC_{ph}$	0.25%	3.40%	5.12%	1.70%	0.56%	0.10%
$GC_{sp}+WL+XC+GC_{ph}$	0.20%	1.09%	4.55%	0.11%	0.21%	0.09%

that is $\Omega_{rc} < 0.072$ in the optimistic setting. While for the pessimistic case Ω_{rc} is unconstrained regardless of the probe we consider because the fiducial parameter is very close to Λ CDM and we do not have enough nonlinear information. To examine this, we have considered the linear power spectrum: we find that the derivative with respect to $\log_{10} \Omega_{rc}$ approaches 0 in the Λ CDM limit, and $P'_L|_{10^{-6}} \approx 0.0002$ compared to $P'_L|_{0.25} \approx 0.08$, where a prime here denotes a derivative with respect to $\log_{10} \Omega_{rc}$. This leads us to conclude that the pessimistic case is still too dominated by linear structure information to constrain Ω_{rc} when

we are close to the Λ CDM limit. It should also be noted that in Bose et al. (2020) the authors do find meaningful constraints using cosmic shear with the same scale cuts we employ in our pessimistic case, but they use a full Markov chain Monte Carlo (MCMC) approach to a Λ CDM fiducial data vector, sampling in Ω_{rc} , as well as employing a different covariance and binning scheme. Additionally it is known that the results obtained by using a Fisher approach can be different from those computed with MCMC method though the sampled parameter is the same (Perotto et al. 2006; Wolz et al. 2012). Therefore a direct comparison

of results is not straightforward. Lastly, our loss in sensitivity in the Λ CDM limit justifies the tight upper limit in nDGP1 when compared to the nDGP2 one.

Moreover a cut in the maximum multipole and scale at lower values, as it is for the pessimistic (or quasi-linear) scenario, leads to larger uncertainties on the model parameter ($\log_{10} \Omega_{\text{rc}}$) compared to the optimistic setting as shown in Table 3 and in Figure 2, where the impact of the different scales adopted is highlighted. On the contrary, the relative errors on the cosmological parameters only slightly deteriorate. This means that most of the power of *Euclid* in constraining this model comes from the nonlinear scales.

Finally, in this analysis we have performed the forecasts on the logarithm of Ω_{rc} following the motivation discussed in Sect. 5, however we tested that a similar constraining power can be obtained by sampling Ω_{rc} directly. For the 3x2pt in the optimistic setting we obtain for the nDGP1: a 24% constraint with respect to the 32% obtained on Ω_{rc} indirectly from the log sampling.

5.3. *k*-mouflage

Here we present our results for the KM model with the two fiducial choices of the $\epsilon_{2,0}$ parameter (KM1 $\epsilon_{2,0} = -0.04$ and KM2 $\epsilon_{2,0} = -0.0001$). The KM1 model represents an extreme case allowed within 95.4% confidence interval by current cosmological data, while KM2 is practically indistinguishable from Λ CDM. Shown in Fig. 5 are the forecast 68.3% and 95.4% joint marginal error contours on cosmological and model parameters for the optimistic scenario. Fig. A.3 shows forecast results for the same models in the pessimistic scenario. The 68.3% errors for both the optimistic and pessimistic configurations are reported in Table 4.

In the optimistic setting, we find that *Euclid* will be able to constrain the modified-gravity parameter $\epsilon_{2,0}$ as follows:

- KM1 :
 - at 5% for the GC_{sp} alone;
 - at 0.15% when considering the combination $\text{WL}+\text{XC}+\text{GC}_{\text{ph}}$;
 - at 0.14% for $\text{GC}_{\text{sp}}+\text{WL}+\text{XC}+\text{GC}_{\text{ph}}$.
- KM2:
 - none of the combinations of probes we consider are able to constrain KM2;
 - upper bound at 8×10^{-4} for the GC_{sp} alone;
 - upper bound at 7×10^{-4} when considering the combination $\text{WL}+\text{XC}+\text{GC}_{\text{ph}}$;
 - upper bound at 6×10^{-4} for $\text{GC}_{\text{sp}}+\text{WL}+\text{XC}+\text{GC}_{\text{ph}}$.

Considering the KM1 fiducial, the optimistic configuration will allow us to constrain $\epsilon_{2,0}$ to $\sim 5\%$ accuracy, using GC_{sp} alone. In the worst case scenario of cutting the observed galaxy power spectrum at $k_{\text{max}} = 0.15 h \text{Mpc}^{-1}$, the error on $\epsilon_{2,0}$ increases to $\sim 11\%$. The constraining power greatly improves when considering the combination $\text{WL}+\text{XC}+\text{GC}_{\text{ph}}$, with percentage error on $\epsilon_{2,0}$ lowering to 0.15% in the optimistic case, with no substantial worsening in the pessimistic scenario. Among the cosmological parameters varied for the KM1 model, $\epsilon_{2,0}$ is the most tightly constrained by the combination $\text{WL}+\text{XC}+\text{GC}_{\text{ph}}$. This shows that this combination of data is well suited to capture the modification induced by *k*-mouflage to the Poisson and lensing equations, probing μ and Σ independently. Moreover the *Euclid* survey will probe the redshift range $z \gtrsim 1$ where the largest effect determined by the running of Newton's constant is expected to manifest (see, e.g., Benevento et al.

2019). We note that the addition of GC_{sp} to $\text{WL}+\text{XC}+\text{GC}_{\text{ph}}$ does not improve constraints on $\epsilon_{2,0}$ in both the pessimistic and optimistic scenarios.

The percentage error on $\epsilon_{2,0}$ in the Λ CDM-proximate KM2 fiducial model goes from 760% using GC_{sp} alone to a value of 464% with the full combination of $\text{GC}_{\text{sp}}+\text{WL}+\text{XC}+\text{GC}_{\text{ph}}$, in the best case scenario. This tells us that, in the optimistic case, the *Euclid* survey will be able to detect a deviation from Λ CDM only if $|\epsilon_{2,0}| \gtrsim 6 \times 10^{-4}$, improving over the constraining power of present CMB and LSS data by somewhat more than one order of magnitude.

From Fig. 5 we notice that $\epsilon_{2,0}$ is anti-correlated with the h parameter. This correlation can be exploited to reduce the Hubble tension, as noticed in Benevento et al. (2019). This effect determines a lower forecast error for the h parameter in the KM1 fiducial model, for which $\epsilon_{2,0}$ is tightly constrained by *Euclid* probes, especially when the full data combination is considered. A similar argument applies for the $\Omega_{\text{m},0}$ parameter which is also better constrained in the KM1 case. The uncertainties for the other parameters do not vary sensibly with the fiducial choice of $\epsilon_{2,0}$.

6. Conclusions

We have explored the constraining power of the future *Euclid* mission for linearly scale-independent extensions of the concordance cosmological model, i.e. models that induce modifications to the linear growth of perturbations that are solely time-dependent, while featuring different testable types of screening mechanisms at smaller nonlinear scales. We considered three specific models, namely JBD, a scalar-tensor theory with a standard kinetic term and a flat potential (Sect. 2.1); the nDGP gravity, a braneworld model in which our Universe is a four-dimensional brane embedded in a five-dimensional Minkowski space-time (Sect. 2.2); and KM gravity, an extension of *k*-essence scenarios with a universal coupling of the scalar field to matter (Sect. 2.3).

We derived forecasts from *Euclid* spectroscopic and photometric primary probes on the cosmological parameters and the extra parameters of the models, respectively, $\log_{10} \omega_{\text{BD}}$ for JBD, $\log_{10} \Omega_{\text{rc}}$ for nDGP and ϵ_2 for KM. In order to do so, we applied the Fisher matrix method to weak lensing (WL); photometric galaxy clustering (GC_{ph}); spectroscopic galaxy clustering (GC_{sp}) and the cross-correlation (XC) between GC_{ph} and WL. For each MG model we considered two fiducial values for the corresponding model parameter, following the rationale of having a case which is representative of the Λ CDM limit and another which differs more significantly while still being (nearly) compatible with current bounds. We modelled the nonlinear matter power spectrum using different prescriptions for each MG model: the HMCODE (Mead et al. 2015, 2016) calibrated on a suite of *N*-body simulations from modified versions of COLA (Tassev et al. 2013; Winther et al. 2017) and RAMSES (Teyssier 2002) for JBD; the halo model reaction (Cataneo et al. 2019) for nDGP; and an analytical approach that combined 1-loop perturbation theory with a halo model for KM following Brax & Valageas (2014); Brax et al. (2015).

When setting the *Euclid* survey specifications, we defined three scenarios, characterized by different cuts in the maximum multipole and wavenumber, to assess the constraining power of nonlinear scales: the quasi-linear with $k_{\text{max}} = 0.155 h \text{Mpc}^{-1}$ for GC_{sp} ; the pessimistic with $k_{\text{max}} = 0.25 h \text{Mpc}^{-1}$ for GC_{sp} , $\ell_{\text{max}} = 1500$ for WL and $\ell_{\text{max}} = 750$ for GC_{ph} ; the optimistic with $k_{\text{max}} = 0.3 h \text{Mpc}^{-1}$ for GC_{sp} , $\ell_{\text{max}} = 5000$ for WL and

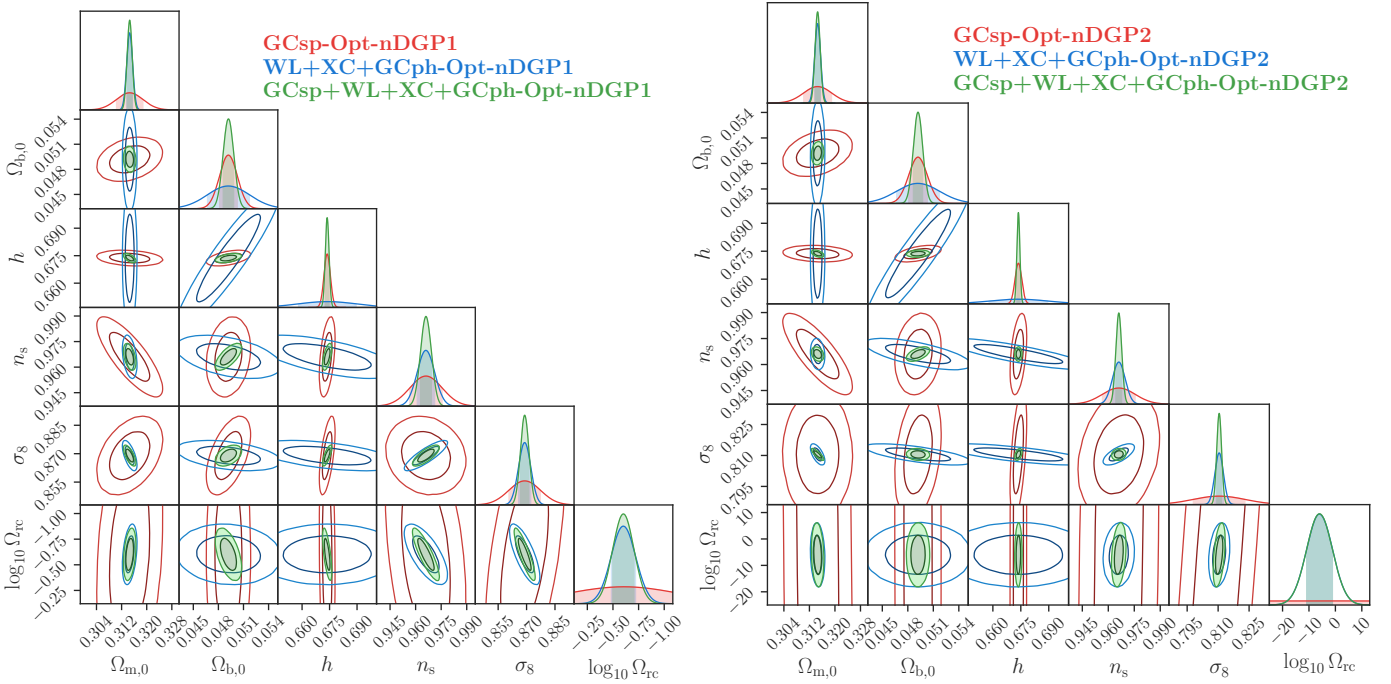


Fig. 4. 68.3% and 95.4% joint marginal error contours on the cosmological parameters for nDGP1 (left panel) and nDGP2 (right panel) in the optimistic case. In red GC_{sp} , in blue $WL+XC+GC_{ph}$ and in green $GC_{sp}+WL+XC+GC_{ph}$.

Table 3. Forecast 1σ marginal errors on the cosmological and model parameters, relative to their corresponding fiducial value, for nDGP1 and nDGP2 in the pessimistic, quasi-linear and optimistic cases, using *Euclid* observations of GC_{sp} , $WL+XC+GC_{ph}$ and $GC_{sp}+WL+XC+GC_{ph}$.

nDGP1 $\Omega_{rc} = 0.25$						
	$\Omega_{m,0}$	$\Omega_{b,0}$	$\log_{10} \Omega_{rc}$	h	n_s	σ_8
Pessimistic setting						
GC_{sp} ($k_{max} = 0.15 h \text{ Mpc}^{-1}$) (quasi-linear)	2.23%	4.30%	142.20%	0.57%	1.69%	1.55%
GC_{sp} ($k_{max} = 0.25 h \text{ Mpc}^{-1}$)	1.41%	2.43%	97.63%	0.30%	1.12%	1.04%
$WL+XC+GC_{ph}$	1.13%	5.64%	49.59%	2.65%	0.92%	1.08%
$GC_{sp}+WL+XC+GC_{ph}$	0.55%	1.95%	40.27%	0.26%	0.68%	0.46%
Optimistic setting						
GC_{sp} ($k_{max} = 0.3 h \text{ Mpc}^{-1}$)	1.33%	2.15%	90.06%	0.25%	0.97%	0.95%
$WL+XC+GC_{ph}$	0.30%	5.08%	19.59%	2.33%	0.52%	0.37%
$GC_{sp}+WL+XC+GC_{ph}$	0.25%	1.28%	16.99%	0.15%	0.33%	0.26%
nDGP2 $\Omega_{rc} = 10^{-6}$						
Pessimistic setting						
GC_{sp} ($k_{max} = 0.15 h \text{ Mpc}^{-1}$) (quasi-linear)	2.36%	4.51%	3020.58%	0.59%	1.68%	2.52%
GC_{sp} ($k_{max} = 0.25 h \text{ Mpc}^{-1}$)	1.46%	2.51%	1923.03%	0.31%	1.10%	1.68%
$WL+XC+GC_{ph}$	0.86%	5.61%	398.64%	2.65%	0.81%	0.58%
$GC_{sp}+WL+XC+GC_{ph}$	0.89%	1.84%	378.82%	0.22%	1.01%	0.39%
Optimistic setting						
GC_{sp} ($k_{max} = 0.3 h \text{ Mpc}^{-1}$)	1.38%	2.21%	1801.03%	0.26%	0.97%	1.54%
$WL+XC+GC_{ph}$	0.29%	5.08%	81.02%	2.32%	0.37%	0.25%
$GC_{sp}+WL+XC+GC_{ph}$	0.25%	1.12%	80.83%	0.12%	0.17%	0.14%

$\ell_{max} = 3000$ for GC_{ph} . In Sect. 5 we have reported in great detail, and discussed, the results corresponding to these different scenarios; for each case, we considered three different combinations of data: GC_{sp} only, $WL+XC+GC_{ph}$ and the full $GC_{sp}+WL+XC+GC_{ph}$. For each of such combinations we presented the relative errors on the fiducial values of the three models as they can give us a glimpse into possible future detections of non-zero modified gravity parameters.

With the full set of probes, we found that, in the optimistic scenario, *Euclid* alone will be able to constrain the JBD param-

eter $\omega_{BD} = 800^{+200}_{-160}$ in the fiducial case JBD1 for the full combination of probes, and in the JBD2 case $\omega_{BD} = 2500^{+1070}_{-750}$. These indicate that *Euclid* alone will be capable of detecting at statistically significant level only values of ω_{BD} which are compatible with current bounds from CMB and LSS. While we found that in the pessimistic case the combination of all probes can be less constraining than that of the photometric ones; this is to be attributed to the cut $z < 0.9$ that we apply to GC_{ph} and XC in the full data combination for the pessimistic scenario and which removes the constraining power of the photometric part at

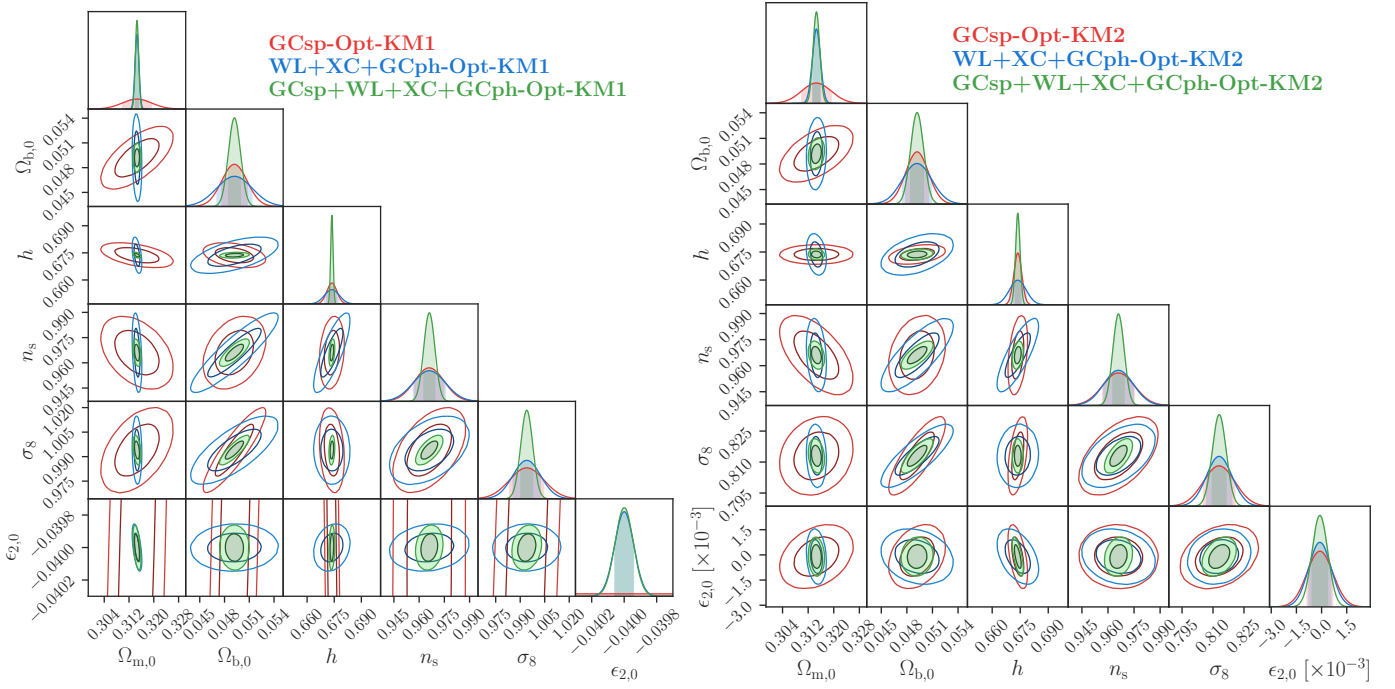


Fig. 5. 68.3% and 95.4% joint marginal error contours on the cosmological parameters for KM1 (left panel) and KM2 (right panel) in the optimistic case. In red GC_{sp} , in blue $WL+XC+GC_{ph}$ and in green $GC_{sp}+WL+XC+GC_{ph}$.

Table 4. Forecast 1σ marginal errors on the cosmological and model parameters, relative to their corresponding fiducial value, for KM1 and KM2 in the pessimistic, quasi-linear and optimistic cases, using *Euclid* observations of GC_{sp} , $WL+XC+GC_{ph}$ and $GC_{sp}+WL+XC+GC_{ph}$.

KM1 $\epsilon_{2,0} = -0.04$						
	$\Omega_{m,0}$	$\Omega_{b,0}$	$\epsilon_{2,0}$	h	n_s	σ_8
Pessimistic setting						
GC_{sp} ($k_{max} = 0.15 h \text{ Mpc}^{-1}$) (quasi-linear)	2.68%	5.34%	11.14%	1.42%	1.48%	1.48%
GC_{sp} ($k_{max} = 0.25 h \text{ Mpc}^{-1}$)	1.57%	3.22%	5.77%	0.52%	1.02%	1.08%
$WL+XC+GC_{ph}$	0.36%	7.36%	0.22%	1.40%	1.93%	1.10%
$GC_{sp}+WL+XC+GC_{ph}$	0.34%	1.73%	0.22%	0.14%	0.60%	0.52%
Optimistic setting						
GC_{sp} ($k_{max} = 0.3 h \text{ Mpc}^{-1}$)	1.48%	3.08%	4.99%	0.41%	0.89%	1.04%
$WL+XC+GC_{ph}$	0.20%	4.30%	0.15%	0.59%	0.98%	0.84%
$GC_{sp}+WL+XC+GC_{ph}$	0.17%	1.47%	0.14%	0.10%	0.34%	0.36%
KM2 $\epsilon_{2,0} = -0.0001$						
Pessimistic setting						
GC_{sp} ($k_{max} = 0.15 h \text{ Mpc}^{-1}$) (quasi-linear)	2.99%	5.61%	1264.58%	0.77%	1.63%	1.15%
GC_{sp} ($k_{max} = 0.25 h \text{ Mpc}^{-1}$)	1.60%	3.08%	824.38%	0.38%	1.07%	0.98%
$WL+XC+GC_{ph}$	1.18%	5.22%	939.23%	1.03%	1.51%	1.17%
$GC_{sp}+WL+XC+GC_{ph}$	0.68%	1.90%	645.16%	0.28%	0.79%	0.67%
Optimistic setting						
GC_{sp} ($k_{max} = 0.3 h \text{ Mpc}^{-1}$)	1.45%	2.69%	759.45%	0.31%	0.94%	0.93%
$WL+XC+GC_{ph}$	0.40%	3.43%	658.67%	0.66%	0.87%	0.75%
$GC_{sp}+WL+XC+GC_{ph}$	0.32%	1.52%	464.38%	0.18%	0.34%	0.41%

lower redshift. This cut impacts the JBD model, given that the latter does not have a screening mechanism and nonlinear scales (which are captured by GC_{ph}) provide therefore quite stringent constraints.

For the nDGP model, we get for the optimistic scenario that $\Omega_{rc} = 0.25^{+0.07}_{-0.05}$ with the full combination in the nDGP1 fiducial case, while for the nDGP2 fiducial ($\Omega_{rc} = 10^{-6}$) we find that $\Omega_{rc} < 0.072$. Furthermore, nDGP2 case is closer to the Λ CDM model than the KM2 one, which is why nDGP2 has worse constraints compared to KM2.

For the KM scenario, we get constraints for the full combination of probes in the fiducial KM1 case of $\epsilon_{2,0} = -0.04 \pm 0.0056$. Out of the full set of cosmological plus model parameters, $\epsilon_{2,0}$ is the most tightly constrained one for KM1 by the full combination, thanks to the independent constraints on clustering and lensing, probing the running of Newton's constant in the range $z \gtrsim 1$ where the largest effect is expected. The KM2 fiducial model (with $\epsilon_{2,0} = -0.0001$) is unconstrained for all the different combinations of probes.

Although it has been shown that for values close to the Λ CDM limit, the nDGP2 and KM2 models remain unconstrained in the pessimistic setting, it is remarkable how *Euclid* alone can significantly reduce the allowed space for these models. For the full probe combination ($GC_{sp}+WL+XC+GC_{ph}$) nDGP2 upper bound at $\Omega_{rc} < 0.072$ for the optimistic scenario significantly improves the current constraints derived with the same approach and similar type of data. This is consistent with the results found in Bose et al. (2020).

The forecasts for KM2 give $|\epsilon_{2,0}| < 5.6 \times 10^{-4}$ in the optimistic case and $|\epsilon_{2,0}| < 7.5 \times 10^{-4}$ in the pessimistic, improving by more than one order of magnitude, even in the pessimistic case, the current constraints from a combination of different cosmological datasets (Benevento et al. 2019). In addition, *Euclid* alone will provide constraints on ω_{BD} which will be tighter than those obtained by a combination of current CMB and low-redshift data Joudaki et al. (2022).

Finally, our analysis clearly showed that most of the constraining power of *Euclid* comes from the nonlinear scales. We conclude that *Euclid* will be able to provide outstanding constraints on extensions beyond the concordance model given a good modelling of our theoretical observables at these scales, like the one used in this analysis, seen from the substantial differences in constraining power between the optimistic and pessimistic case. Additionally we would like to stress that the combination and cross-correlation of future *Euclid* data with CMB measurements will be of crucial importance for cosmological constraints of extended models. As already shown within the *Euclid* Collaboration (Euclid Collaboration: Ilić et al. 2022) the improvements in the constraints when cross-correlation of *Euclid* with CMB data is considered can be of the order of two to three and in some cases even larger. A large effort is currently ongoing to extend this analysis to other extended models including those in this work.

Acknowledgements. The Euclid Consortium acknowledges the European Space Agency and a number of agencies and institutes that have supported the development of *Euclid*, in particular the Academy of Finland, the Agenzia Spaziale Italiana, the Belgian Science Policy, the Canadian Euclid Consortium, the French Centre National d'Etudes Spatiales, the Deutsches Zentrum für Luft- und Raumfahrt, the Danish Space Research Institute, the Fundação para a Ciência e a Tecnologia, the Ministerio de Ciencia e Innovación, the National Aeronautics and Space Administration, the National Astronomical Observatory of Japan, the Nederlandse Onderzoekschool Voor Astronomie, the Norwegian Space Agency, the Romanian Space Agency, the State Secretariat for Education, Research and Innovation (SERI) at the Swiss Space Office (SSO), and the United Kingdom Space Agency. A complete and detailed list is available on the *Euclid* web site (<http://www.euclid-ec.org>). B.B. and L.L. were supported by a Swiss National Science Foundation Professorship grant (Nos. 170547 & 202671). E.B. has received funding from the European Union's Horizon 2020 research and innovation programme under the Marie Skłodowska-Curie grant agreement No 754496. B.B. was supported by a UK Research and Innovation Stephen Hawking Fellowship (EP/W005654/2). P.G.F. acknowledges funding from STFC, the Beecroft Trust and the European Research Council (ERC) under the European Unions Horizon 2020 research and innovation programme (grant agreement No 693024). N.F. is supported by the Italian Ministry of University and Research (MUR) through Rita Levi Montalcini project "Tests of gravity at cosmological scales" with reference PGR19ILFGP. N.F., F.P. and A.R.F. also acknowledge the FCT project with ref. number PTDC/FIS-AST/0054/2021. K.K. is supported by the UK STFC grant ST/S000550/1 and ST/W001225/1. For the purpose of open access, the author(s) has applied a Creative Commons Attribution (CC BY) licence to any Author Accepted Manuscript version arising. F.P. acknowledges partial support from the INFN grant InDark and the Departments of Excellence grant L.232/2016 of the Italian Ministry of University and Research (MUR). A.R.F. acknowledges support from DL 57/2016 from the 'Departamento de Física, Faculdade de Ciências, Universidade de Lisboa'. I.T. acknowledges funding from the European Research Council (ERC) under the European Union's Horizon 2020 research and innovation programme (Grant agreement No. 863929; project title "Testing the law of gravity with novel large-scale structure observables" and acknowledges support from the Spanish Ministry of Science, Innovation and Universities through grant ESP2017-89838, and the H2020 programme of the

European Commission through grant 776247. Z.S. acknowledges funding from DFG project 456622116.

Appendix A: Further results

In this Appendix we show additional results to complement what has been discussed in Sect. 5. In Figs. A.1, A.2 and A.3 we provide the 68.3% and 95.4% joint marginal error contours in the pessimistic case on the cosmological parameters for the JBD, nDGP and KM respectively. We also include Fig. A.4 for the JBD case in the pessimistic scenario without the cut at $z < 0.9$. As discussed in Sect. 5.1 the combination of all probes in the pessimistic scenario might result in worse constraints for some parameters with respect to the combination WL+XC+GC_{ph} because in the former we perform a cut in redshift to avoid overlap between XC and GC_{ph} with GC_{sp}. Comparing Figs. A.1 and 5.1 we conclude that the z-cut removes the constraining power of the photometric part. In detail, without z-cut we have the following forecast 68.3% relative error for GC_{sp}+WL+XC+GC_{ph}:

$$\begin{aligned} - \text{JBD1:} & \quad \{\Omega_{m,0}, \Omega_{b,0}, \log_{10} \omega_{\text{BD}}, h, n_s, \sigma_8\} & = \\ & \quad \{0.36\%, 1.28\%, 9.95\%, 0.20\%, 0.44\%, 0.29\%\}, \\ - \text{JBD2:} & \quad \{\Omega_{m,0}, \Omega_{b,0}, \log_{10} \omega_{\text{BD}}, h, n_s, \sigma_8\} & = \\ & \quad \{0.33\%, 1.26\%, 16.55\%, 0.17\%, 0.39\%, 0.24\%\}. \end{aligned}$$

References

Aghanim, N., Akrami, Y., Ashdown, Y., et al. 2020, *A&A*, 641, A6, [Erratum: *A&A*, 652, C4 (2021)]
 Avilez, A. & Skordis, C. 2014, *PhRvL*, 113, 011101
 Babichev, E., Deffayet, C., & Ziour, R. 2009, *IJMPD*, 18, 2147
 Bag, S., Mishra, S. S., & Sahni, V. 2018, *PhRvD*, 97, 123537
 Ballardini, M., Braglia, M., Finelli, F., et al. 2020, *JCAP*, 10, 044
 Ballardini, M., Finelli, F., & Sapone, D. 2022, *JCAP*, 06, 004
 Ballardini, M., Finelli, F., Umiltà, C., & Paoletti, D. 2016, *JCAP*, 05, 067
 Ballardini, M., Sapone, D., Umiltà, C., et al. 2019, *JCAP*, 05, 049
 Bardeen, J. M. 1980, *PhRvD*, 22, 1882
 Barreira, A., Brax, P., Clesse, S., et al. 2015, *PhRvD*, 91, 063528
 Barreira, A., Sánchez, A. G., & Schmidt, F. 2016, *PhRvD*, 94, 084022
 Bellini, E., Barreira, A., Frusciante, N., et al. 2018, *PhRvD*, 97, 023520
 Bellini, E., Sawicki, I., & Zumalacárregui, M. 2020, *JCAP*, 02, 008
 Benevento, G., Raveri, M., Lazanu, A., et al. 2019, *JCAP*, 05, 027
 Berti, E., Barausse, E., Cardoso, V., et al. 2015, *CQGra*, 32, 243001
 Bertotti, B., Iess, L., & Tortora, P. 2003, *Natur*, 425, 374
 Blas, D., Lesgourgues, J., & Tram, T. 2011, *JCAP*, 07, 034
 Boisseau, B., Esposito-Farese, G., Polarski, D., & Starobinsky, A. A. 2000, *PhRvL*, 85, 2236
 Bose, B., Cataneo, M., Tröster, T., et al. 2020, *MNRAS*, 498, 4650
 Bose, B., Wright, B. S., Cataneo, M., et al. 2021, *MNRAS*, 508, 2479
 Bowcock, P., Charmousis, C., & Gregory, R. 2000, *CQGra*, 17, 4745
 Braglia, M., Ballardini, M., Emond, W. T., et al. 2020, *PhRvD*, 102, 023529
 Braglia, M., Ballardini, M., Finelli, F., & Koyama, K. 2021, *PhRvD*, 103, 043528
 Brans, C. & Dicke, R. H. 1961, *PhRv*, 124, 925
 Brax, P., Casas, S., Desmond, H., & Elder, B. 2021, *Univ*, 8, 11
 Brax, P., Rizzo, L. A., & Valageas, P. 2015, *PhRvD*, 92, 043519
 Brax, P. & Valageas, P. 2013, *PhRvD*, 88, 023527
 Brax, P. & Valageas, P. 2014, *PhRvD*, 90, 023508
 Brax, P. & Valageas, P. 2016, *JCAP*, 01, 020
 Bullock, J. S., Kolatt, T. S., Sigad, Y., et al. 2001, *MNRAS*, 321, 559
 Cardoso, A., Koyama, K., Seahra, S. S., & Silva, F. P. 2008, *PhRvD*, 77, 083512
 Carroll, S. M., Duvvuri, V., Trodden, M., & Turner, M. S. 2004, *PhRvD*, 70, 043528
 Casas, S. et al. 2023 [arXiv:2306.11053]
 Cataneo, M., Lombriser, L., Heymans, C., et al. 2019, *MNRAS*, 488, 2121
 Cataneo, M., Uhlemann, C., Arnold, C., et al. 2022, *MNRAS*, 513, 1623
 Charmousis, C., Gregory, R., Kaloper, N., & Padilla, A. 2006, *JHEP*, 10, 066
 Cheng, G., Wu, F., & Chen, X. 2021, *PhRvD*, 103, 103527
 Cooray, A. & Sheth, R. K. 2002, *PhR*, 372, 1
 Deffayet, C. 2001, *PhLB*, 502, 199
 Dvali, G. R., Gabadadze, G., & Porrati, M. 2000, *PhLB*, 485, 208
 Eisenstein, D. J., Seo, H.-j., & White, M. J. 2007, *ApJ*, 664, 660
 Euclid Collaboration: Blanchard, A., Camera, S., Carbone, C., et al. 2020, *A&A*, 642, A191
 Euclid Collaboration: Ilić, S., Aghanim, N., Baccigalupi, C., et al. 2022, *A&A*, 657, A91
 Ferreira, P. G. 2019, *ARA&A*, 57, 335
 Gorbunov, D., Koyama, K., & Sibiryakov, S. 2006, *PhRvD*, 73, 044016

Hernández-Aguayo, C., Ruan, C.-Z., Li, B., et al. 2022, *JCAP*, 01, 048
 Hojjati, A., Pogosian, L., & Zhao, G.-B. 2011, *JCAP*, 1108, 005
 Hu, B., Raveri, M., Frusciante, N., & Silvestri, A. 2014, *PhRvD*, 89, 103530
 Hu, W. & Sawicki, I. 2007a, *PhRvD*, 76, 104043
 Hu, W. & Sawicki, I. 2007b, *PhRvD*, 76, 064004
 Joudaki, S., Blake, C., Johnson, A., et al. 2018, *MNRAS*, 474, 4894
 Joudaki, S., Ferreira, P. G., Lima, N. A., & Winther, H. A. 2022, *PhRvD*, 105, 043522
 Khoury, J. & Weltman, A. 2004, *PhRvL*, 93, 171104
 Koyama, K. & Maartens, R. 2006, *JCAP*, 01, 016
 Lee, S. et al. 2021, *MNRAS*, 509, 4982
 Lesgourgues, J. 2011 [arXiv:1104.2932]
 Lewis, A., Challinor, A., & Lasenby, A. 2000, *ApJ*, 538, 473
 Liu, R., Valogiannis, G., Battaglia, N., & Bean, R. 2021, *PhRvD*, 104, 103519
 Lombriser, L., Hu, W., Fang, W., & Seljak, U. 2009, *PhRvD*, 80, 063536
 Lombriser, L., Yoo, J., & Koyama, K. 2013, *PhRvD*, 87, 104019
 Luty, M. A., Porrati, M., & Rattazzi, R. 2003, *JHEP*, 09, 029
 Ma, C.-P. & Bertschinger, E. 1995, *ApJ*, 455, 7
 Mead, A., Brieden, S., Tröster, T., & Heymans, C. 2021, *MNRAS*, 502, 1401
 Mead, A., Heymans, C., Lombriser, L., et al. 2016, *MNRAS*, 459, 1468
 Mead, A., Peacock, J., Heymans, C., Joudaki, S., & Heavens, A. 2015, *MNRAS*, 454, 1958
 Mueller, E.-M., Percival, W., Linder, E., et al. 2018, *MNRAS*, 475, 2122
 Navarro, J. F., Frenk, C. S., & White, S. D. M. 1997, *ApJ*, 490, 493
 Ooba, J., Ichiki, K., Chiba, T., & Sugiyama, N. 2017, *PTEP*, 2017, 043E03
 Pace, F., Battye, R., Bellini, E., et al. 2021, *JCAP*, 06, 017
 Perotto, L., Lesgourgues, J., Hannestad, S., Tu, H., & Wong, Y. Y. 2006, *JCAP*, 10, 013
 Raccanelli, A., Bertacca, D., Pietrobon, D., et al. 2013, *MNRAS*, 436, 89
 Raveri, M., Hu, B., Frusciante, N., & Silvestri, A. 2014, *PhRvD*, 90, 043513
 Raveri, M., Pogosian, L., Martinelli, M., et al. 2021 [arXiv:2107.12990]
 Rossi, M., Ballardini, M., Braglia, M., et al. 2019, *PhRvD*, 100, 103524
 Schmidt, F. 2009, *PhRvD*, 80, 123003
 Schneider, A., Refregier, A., Grandis, S., et al. 2020a, *JCAP*, 04, 020
 Schneider, A., Stoira, N., Refregier, A., et al. 2020b, *JCAP*, 04, 019
 Seahra, S. S. & Hu, W. 2010, *PhRvD*, 82, 124015
 Sheth, R. K. & Tormen, G. 1999, *MNRAS*, 308, 119
 Sheth, R. K. & Tormen, G. 2002, *MNRAS*, 329, 61
 Song, Y.-S. 2008, *PhRvD*, 77, 124031
 Spurio Mancini, A., Köhlinger, F., Joachimi, B., et al. 2019, *MNRAS*, 490, 2155
 Takahashi, R., Sato, M., Nishimichi, T., Taruya, A., & Oguri, M. 2012, *ApJ*, 761, 152
 Taruya, A., Nishimichi, T., & Saito, S. 2010, *PhRvD*, 82, 063522
 Tassev, S., Zaldarriaga, M., & Eisenstein, D. 2013, *JCAP*, 06, 036
 Teysier, R. 2002, *A&A*, 385, 337
 Touboul, P., Métris, G., Rodrigues, M., et al. 2017, *PhRvL*, 119, 231101
 Umiltà, C., Ballardini, M., Finelli, F., & Paoletti, D. 2015, *JCAP*, 08, 017
 Vainshtein, A. I. 1972, *PhLB*, 39, 393
 Valageas, P., Nishimichi, T., & Taruya, A. 2013, *PhRvD*, 87, 083522
 Voisin, G., Cognard, I., Freire, P. C. C., et al. 2020, *A&A*, 638, A24
 Williams, J. G., Turyshv, S. G., & Boggs, D. 2012, *CQGra*, 29, 184004
 Winther, H. A., Koyama, K., Manera, M., Wright, B. S., & Zhao, G.-B. 2017, *JCAP*, 08, 006
 Wolz, L., Kilbinger, M., Weller, J., & Giannantonio, T. 2012, *JCAP*, 09, 009
 Xu, L. 2014, *JCAP*, 02, 048
 Zhao, G.-B., Pogosian, L., Silvestri, A., & Zylberberg, J. 2009, *PhRvD*, 79, 083513
 Zucca, A., Pogosian, L., Silvestri, A., & Zhao, G.-B. 2019, *JCAP*, 05, 001
 Zumalacárregui, M., Bellini, E., Sawicki, I., et al. 2017, *JCAP*, 08, 019

¹ Department of Physics "E. Pancini", University Federico II, Via Cinthia 6, 80126, Napoli, Italy

² Dipartimento di Fisica, Università degli Studi di Torino, Via P. Giuria 1, 10125 Torino, Italy

³ INFN-Sezione di Torino, Via P. Giuria 1, 10125 Torino, Italy

⁴ INAF-Osservatorio Astrofisico di Torino, Via Osservatorio 20, 10025 Pino Torinese (TO), Italy

⁵ INAF-Osservatorio Astronomico di Roma, Via Frascati 33, 00078 Monteporzio Catone, Italy

⁶ INFN-Sezione di Roma, Piazzale Aldo Moro, 2 - c/o Dipartimento di Fisica, Edificio G. Marconi, 00185 Roma, Italy

⁷ Institute for Theoretical Particle Physics and Cosmology (TTK), RWTH Aachen University, 52056 Aachen, Germany

⁸ Université de Genève, Département de Physique Théorique and Centre for Astroparticle Physics, 24 quai Ernest-Ansermet, CH-1211 Genève 4, Switzerland

⁹ Institute of Space Sciences (ICE, CSIC), Campus UAB, Carrer de Can

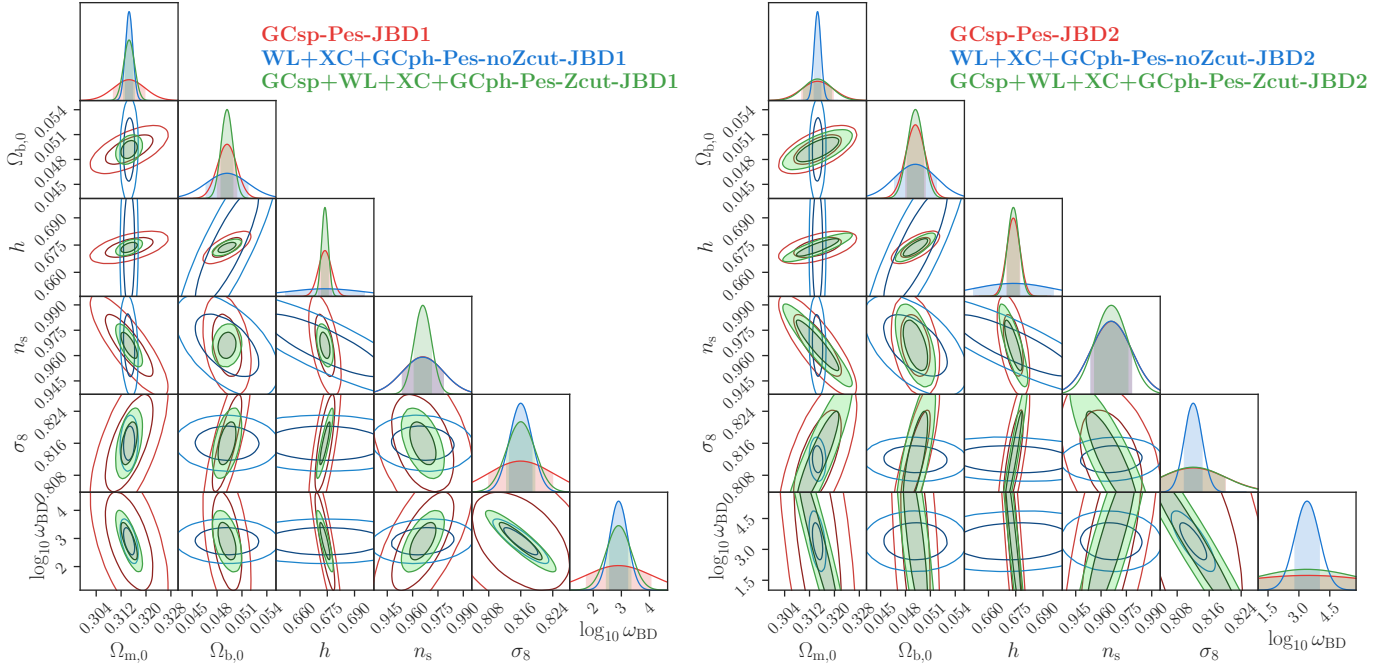


Fig. A.1. 68.3% and 95.4% joint marginal error contours on the cosmological parameters for JBD1 (left panel) and JBD2 (right panel) in the pessimistic case. In red GC_{sp}, in blue WL+XC+GC_{ph} and in green GC_{sp}+WL+XC+GC_{ph}.

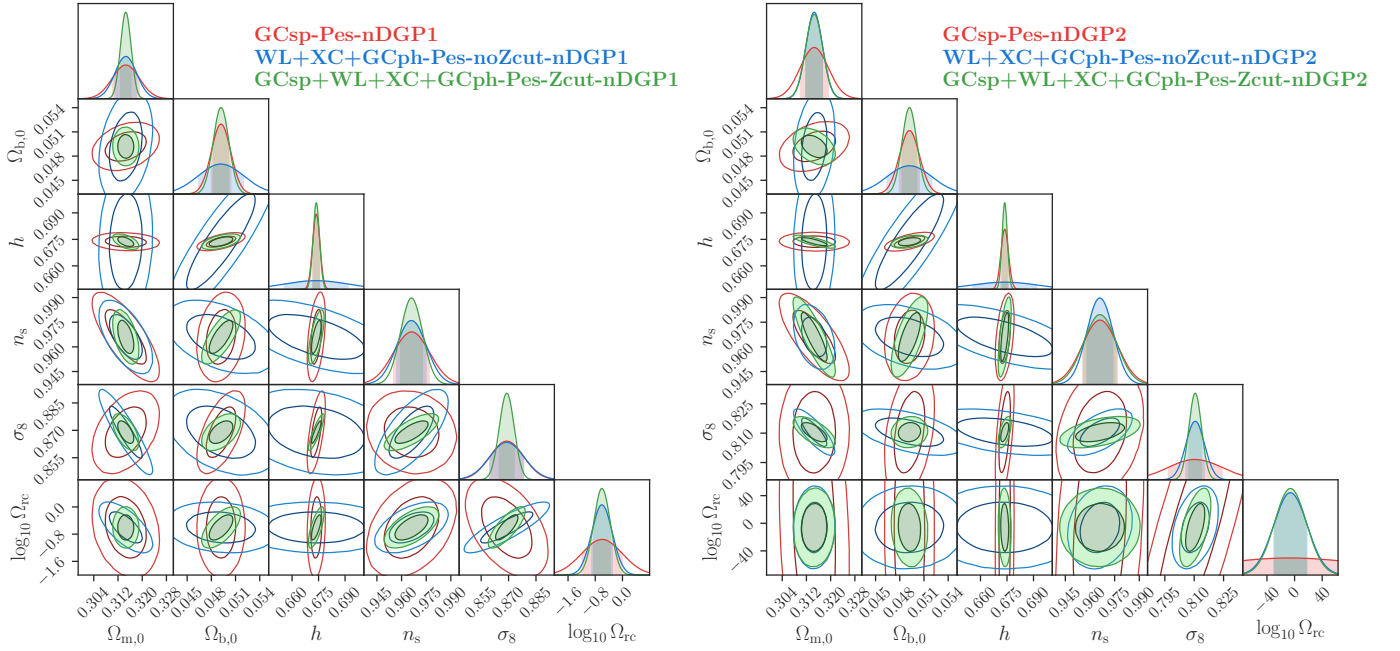


Fig. A.2. 68.3% and 95.4% joint marginal error contours on the cosmological parameters for nDGP1 (left panel) and nDGP2 (right panel) in the pessimistic case. In red GC_{sp}, in blue WL+XC+GC_{ph} and in green GC_{sp}+WL+XC+GC_{ph}.

Magrans, s/n, 08193 Barcelona, Spain

¹⁰ Institut d'Estudis Espacials de Catalunya (IEEC), Carrer Gran Capitá 2-4, 08034 Barcelona, Spain

¹¹ Institut de Recherche en Astrophysique et Planétologie (IRAP), Université de Toulouse, CNRS, UPS, CNES, 14 Av. Edouard Belin, 31400 Toulouse, France

¹² Dipartimento di Fisica e Scienze della Terra, Università degli Studi di Ferrara, Via Giuseppe Saragat 1, 44122 Ferrara, Italy

¹³ Dipartimento di Fisica e Astronomia, Università di Bologna, Via Gobetti 93/2, 40129 Bologna, Italy

¹⁴ INAF-Osservatorio di Astrofisica e Scienza dello Spazio di Bologna, Via Piero Gobetti 93/3, 40129 Bologna, Italy

¹⁵ INFN-Sezione di Bologna, Viale Bertini Pichat 6/2, 40127 Bologna, Italy

¹⁶ INFN, Sezione di Trieste, Via Valerio 2, 34127 Trieste TS, Italy

¹⁷ IFPU, Institute for Fundamental Physics of the Universe, via Beirut 2, 34151 Trieste, Italy

¹⁸ SISSA, International School for Advanced Studies, Via Bonomea 265, 34136 Trieste TS, Italy

¹⁹ Johns Hopkins University 3400 North Charles Street Baltimore, MD 21218, USA

²⁰ Institute for Astronomy, University of Edinburgh, Royal Observatory, Blackford Hill, Edinburgh EH9 3HJ, UK

²¹ Institute for Computational Science, University of Zurich, Win-

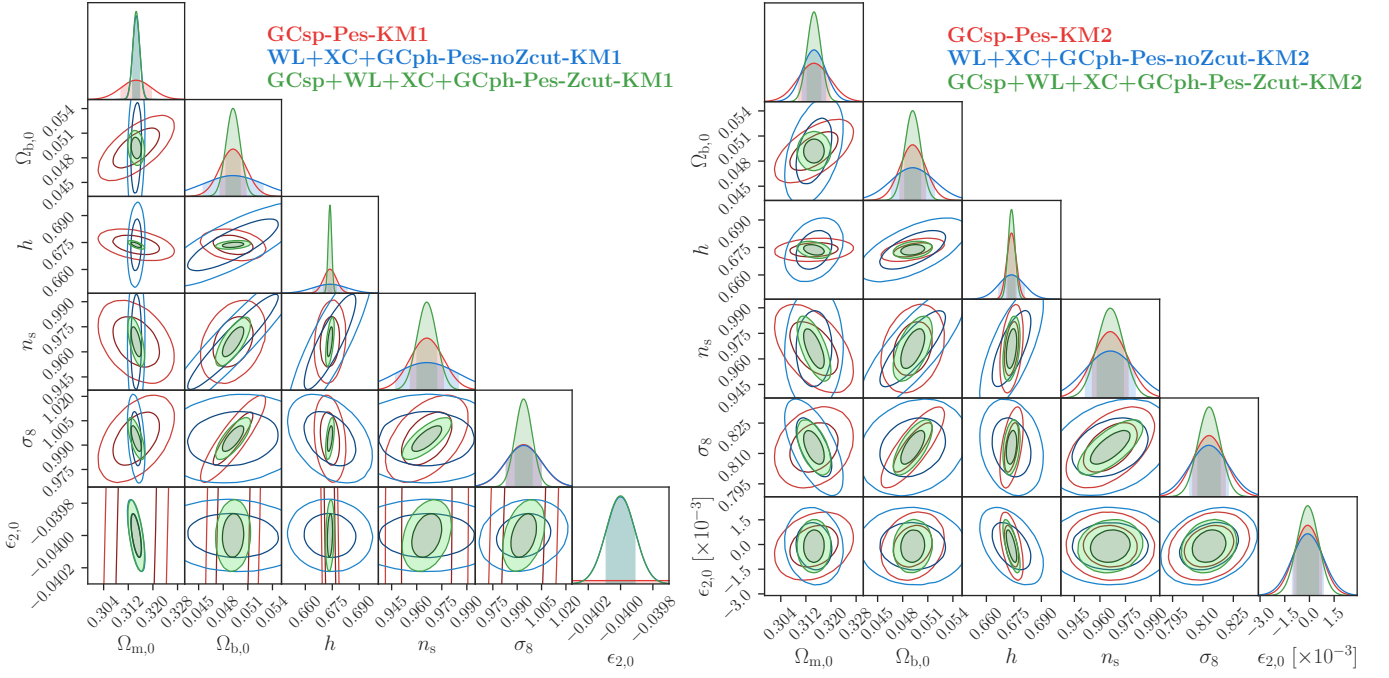


Fig. A.3. 68.3% and 95.4% joint marginal error contours on the cosmological parameters for KM1 (left panel) and KM2 (right panel) in the pessimistic case. In red GC_{sp} , in blue $WL+XC+GC_{ph}$ and in green $GC_{sp}+WL+XC+GC_{ph}$.

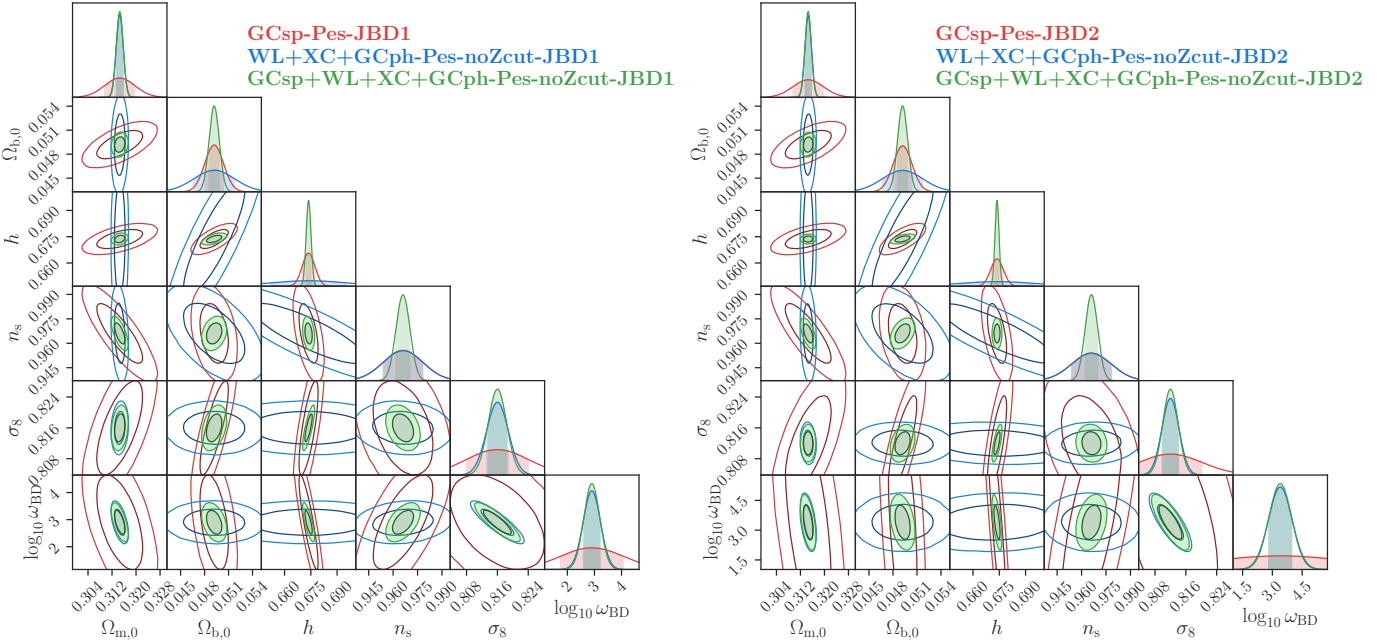


Fig. A.4. 68.3% and 95.4% joint marginal error contours on the cosmological parameters for JBD1 (left panel) and JBD2 (right panel) in the pessimistic case without the redshift cut at $z < 0.9$ (see the text for details). In red GC_{sp} , in blue $WL+XC+GC_{ph}$ and in green $GC_{sp}+WL+XC+GC_{ph}$.

terthurerstrasse 190, 8057 Zurich, Switzerland

²² Institut de Physique Théorique, CEA, CNRS, Université Paris-Saclay 91191 Gif-sur-Yvette Cedex, France

²³ Dipartimento di Fisica e Astronomia "G.Galilei", Università di Padova, Via Marzolo 8, 35131 Padova, Italy

²⁴ INFN-Padova, Via Marzolo 8, 35131 Padova, Italy

²⁵ INAF-Osservatorio Astronomico di Padova, Via dell'Osservatorio 5, 35122 Padova, Italy

²⁶ CERN, Theoretical Physics Department, Geneva, Switzerland

²⁷ Department of Physics, Oxford University, Keble Road, Oxford OX1 3RH, UK

²⁸ INFN-Bologna, Via Irnerio 46, 40126 Bologna, Italy

²⁹ Institute of Cosmology and Gravitation, University of Portsmouth, Portsmouth PO1 3FX, UK

³⁰ Dipartimento di Scienze Matematiche, Fisiche e Informatiche, Università di Parma, Viale delle Scienze 7/A 43124 Parma, Italy

³¹ INFN Gruppo Collegato di Parma, Viale delle Scienze 7/A 43124 Parma, Italy

³² Instituto de Astrofísica e Ciências do Espaço, Faculdade de Ciências, Universidade de Lisboa, Campo Grande, 1749-016 Lisboa, Portugal

³³ Institut d'Astrophysique de Paris, UMR 7095, CNRS, and Sorbonne Université, 98 bis boulevard Arago, 75014 Paris, France

³⁴ Institut für Theoretische Physik, University of Heidelberg, Philosophenweg 16, 69120 Heidelberg, Germany

- ³⁵ Université St Joseph; Faculty of Sciences, Beirut, Lebanon
- ³⁶ Institute Lorentz, Leiden University, PO Box 9506, Leiden 2300 RA, The Netherlands
- ³⁷ Institute of Theoretical Astrophysics, University of Oslo, P.O. Box 1029 Blindern, 0315 Oslo, Norway
- ³⁸ Université Paris-Saclay, CNRS, Institut d'astrophysique spatiale, 91405, Orsay, France
- ³⁹ Mullard Space Science Laboratory, University College London, Holmbury St Mary, Dorking, Surrey RH5 6NT, UK
- ⁴⁰ Dipartimento di Fisica, Università degli studi di Genova, and INFN-Sezione di Genova, via Dodecaneso 33, 16146, Genova, Italy
- ⁴¹ INFN-Sezione di Roma Tre, Via della Vasca Navale 84, 00146, Roma, Italy
- ⁴² INAF-Osservatorio Astronomico di Capodimonte, Via Moiariello 16, 80131 Napoli, Italy
- ⁴³ Instituto de Astrofísica e Ciências do Espaço, Universidade do Porto, CAUP, Rua das Estrelas, PT4150-762 Porto, Portugal
- ⁴⁴ INAF-IASF Milano, Via Alfonso Corti 12, 20133 Milano, Italy
- ⁴⁵ Institut de Física d'Altes Energies (IFAE), The Barcelona Institute of Science and Technology, Campus UAB, 08193 Bellaterra (Barcelona), Spain
- ⁴⁶ Port d'Informació Científica, Campus UAB, C. Albareda s/n, 08193 Bellaterra (Barcelona), Spain
- ⁴⁷ INFN section of Naples, Via Cinthia 6, 80126, Napoli, Italy
- ⁴⁸ Dipartimento di Fisica e Astronomia "Augusto Righi" - Alma Mater Studiorum Università di Bologna, Viale Berti Pichat 6/2, 40127 Bologna, Italy
- ⁴⁹ INAF-Osservatorio Astrofisico di Arcetri, Largo E. Fermi 5, 50125, Firenze, Italy
- ⁵⁰ Centre National d'Etudes Spatiales, Toulouse, France
- ⁵¹ Institut national de physique nucléaire et de physique des particules, 3 rue Michel-Ange, 75794 Paris Cédex 16, France
- ⁵² European Space Agency/ESRIN, Largo Galileo Galilei 1, 00044 Frascati, Roma, Italy
- ⁵³ ESAC/ESA, Camino Bajo del Castillo, s/n., Urb. Villafranca del Castillo, 28692 Villanueva de la Cañada, Madrid, Spain
- ⁵⁴ Univ Lyon, Univ Claude Bernard Lyon 1, CNRS/IN2P3, IP2I Lyon, UMR 5822, 69622, Villeurbanne, France
- ⁵⁵ Institute of Physics, Laboratory of Astrophysics, Ecole Polytechnique Fédérale de Lausanne (EPFL), Observatoire de Sauverny, 1290 Versoix, Switzerland
- ⁵⁶ Departamento de Física, Faculdade de Ciências, Universidade de Lisboa, Edifício C8, Campo Grande, PT1749-016 Lisboa, Portugal
- ⁵⁷ Department of Astronomy, University of Geneva, ch. d'Ecogia 16, 1290 Versoix, Switzerland
- ⁵⁸ Université Paris-Saclay, Université Paris Cité, CEA, CNRS, Astrophysique, Instrumentation et Modélisation Paris-Saclay, 91191 Gif-sur-Yvette, France
- ⁵⁹ INAF-Osservatorio Astronomico di Trieste, Via G. B. Tiepolo 11, 34143 Trieste, Italy
- ⁶⁰ Istituto Nazionale di Fisica Nucleare, Sezione di Bologna, Via Irnerio 46, 40126 Bologna, Italy
- ⁶¹ Max Planck Institute for Extraterrestrial Physics, Giessenbachstr. 1, 85748 Garching, Germany
- ⁶² Universitäts-Sternwarte München, Fakultät für Physik, Ludwig-Maximilians-Universität München, Scheinerstrasse 1, 81679 München, Germany
- ⁶³ Dipartimento di Fisica "Aldo Pontremoli", Università degli Studi di Milano, Via Celoria 16, 20133 Milano, Italy
- ⁶⁴ INFN-Sezione di Milano, Via Celoria 16, 20133 Milano, Italy
- ⁶⁵ INAF-Osservatorio Astronomico di Brera, Via Brera 28, 20122 Milano, Italy
- ⁶⁶ Jet Propulsion Laboratory, California Institute of Technology, 4800 Oak Grove Drive, Pasadena, CA, 91109, USA
- ⁶⁷ von Hoerner & Sulger GmbH, Schloßplatz 8, 68723 Schwetzingen, Germany
- ⁶⁸ Technical University of Denmark, Elektrovej 327, 2800 Kgs. Lyngby, Denmark
- ⁶⁹ Max-Planck-Institut für Astronomie, Königstuhl 17, 69117 Heidelberg, Germany
- ⁷⁰ Aix-Marseille Université, CNRS/IN2P3, CPPM, Marseille, France
- ⁷¹ Department of Physics and Helsinki Institute of Physics, Gustaf Hällströmin katu 2, 00014 University of Helsinki, Finland
- ⁷² NOVA optical infrared instrumentation group at ASTRON, Oude Hoogeveensedijk 4, 7991PD, Dwingeloo, The Netherlands
- ⁷³ Argelander-Institut für Astronomie, Universität Bonn, Auf dem Hügel 71, 53121 Bonn, Germany
- ⁷⁴ Dipartimento di Fisica e Astronomia "Augusto Righi" - Alma Mater Studiorum Università di Bologna, via Piero Gobetti 93/2, 40129 Bologna, Italy
- ⁷⁵ Department of Physics, Institute for Computational Cosmology, Durham University, South Road, DH1 3LE, UK
- ⁷⁶ European Space Agency/ESTEC, Keplerlaan 1, 2201 AZ Noordwijk, The Netherlands
- ⁷⁷ Department of Physics and Astronomy, University of Aarhus, Ny Munkegade 120, DK-8000 Aarhus C, Denmark
- ⁷⁸ Centre for Astrophysics, University of Waterloo, Waterloo, Ontario N2L 3G1, Canada
- ⁷⁹ Department of Physics and Astronomy, University of Waterloo, Waterloo, Ontario N2L 3G1, Canada
- ⁸⁰ Perimeter Institute for Theoretical Physics, Waterloo, Ontario N2L 2Y5, Canada
- ⁸¹ Space Science Data Center, Italian Space Agency, via del Politecnico snc, 00133 Roma, Italy
- ⁸² Institute of Space Science, Bucharest, 077125, Romania
- ⁸³ Instituto de Astrofísica de Canarias, Calle Vía Láctea s/n, 38204, San Cristóbal de La Laguna, Tenerife, Spain
- ⁸⁴ Departamento de Astrofísica, Universidad de La Laguna, 38206, La Laguna, Tenerife, Spain
- ⁸⁵ Departamento de Física, FCFM, Universidad de Chile, Blanco Encalada 2008, Santiago, Chile
- ⁸⁶ Aix-Marseille Université, CNRS, CNES, LAM, Marseille, France
- ⁸⁷ Centro de Investigaciones Energéticas, Medioambientales y Tecnológicas (CIEMAT), Avenida Complutense 40, 28040 Madrid, Spain
- ⁸⁸ Instituto de Astrofísica e Ciências do Espaço, Faculdade de Ciências, Universidade de Lisboa, Tapada da Ajuda, 1349-018 Lisboa, Portugal
- ⁸⁹ Universidad Politécnica de Cartagena, Departamento de Electrónica y Tecnología de Computadoras, 30202 Cartagena, Spain
- ⁹⁰ Kapteyn Astronomical Institute, University of Groningen, PO Box 800, 9700 AV Groningen, The Netherlands
- ⁹¹ Infrared Processing and Analysis Center, California Institute of Technology, Pasadena, CA 91125, USA
- ⁹² Institut d'Astrophysique de Paris, 98bis Boulevard Arago, 75014, Paris, France